Responses to the Editor:

Comments to the author: There are major concerns by one of the referees that should be addressed so please consider these suggestion/clarification for a further review process.

Non-public comments to the Author: There are major concerns by one of the referees that should be addressed so please consider these suggestion/clarification for a further review process.

Response: Thank you for providing us the opportunity to revise and improve our manuscript. We are also grateful for the valuable comments and suggestions by the reviewers. We have addressed all the raised concerns with care. Below are point-to-point responses. Detailed responses to each of the reviewer's comments are provided in blue, and the revised text is underlined. Attached please also find the marked-up manuscript to track the changes in the revised manuscript.

Responses to Referee #3:

No suggestion for revision.

Response: We thank the reviewer for taking the time to assess this manuscript.

Responses to Referee #4:

General comments:

Comments to "The importance of biomass burning in light extinction and direct radiative effect of urban aerosol during the COVID-19 lockdown in Xi'an, China" by Tian et al.

The paper by Tian et al. investigated the impacts of anthropogenic sources on b_{ext} and direct radiative forcing (DRF). They found out that biomass burning dominated b_{ext} and DRF during the COVID-19 lockdown in Xi'an, China. This paper is well-written and topical. However, some important details on the measurement methods and data analysis method are needed. Furthermore, some results require further interpretation. I suggest that this paper will be published in ACP after addressing the points listed below.

Response: We thank the reviewer for the helpful comments and providing us the opportunity to strengthen our research. For the concerns regarding the measurement methods and data analysis method, we have carefully addressed them in the responses of comments (1) and (2). Furthermore, we improved the results and discussion following the reviewer's comments. We hope the revised manuscript facilitates the understanding of the readers. Please see our point-to-point responses as follow.

Comment (1): The mass concentrations of ions, OA were measured in PM_1. In fact, considerable fractions of them might be distributed in $PM_{1\text{-}2.5}$, especially during the polluted period in north China. Thus, ions and OA in $PM_{2.5}$ should be underestimated.

I suggest author reconstruct the $PM_{2.5}$ mass based on these measured chemical compositions to discuss their uncertainties.

Response: We agree with the reviewer that OA and ions concentrations measured in PM_1 might be lower than those in $PM_{2.5}$. We thus have compared the measured $PM_{2.5}$ mass concentration with the sum concentration of POA, LO-OOA, MO-OOA, NH_4NO_3, $(NH_4)_2SO_4$, BC and fine soil (the sum is referred to as the reconstructed PM), following the reviewer's suggestion. We find the measured $PM_{2.5}$ and the reconstructed PM are strongly correlated with an R^2 of 0.86, however, the slope of this linear regression is only 0.79 (Figure S2). That is, the mass concentration of reconstructed PM is 0.79 times of the measured $PM_{2.5}$. In the revised manuscript, we have added the above discussion in the method Sect. 2.4:

> "The reconstructed [PM] ([PM] = [NH_4NO_3] + [$(NH_4)_2SO_4$] + [POA] + [LO-OOA] + [MO-OOA] + [BC] + [fine soil]) is strongly correlated with the measured [$PM_{2.5}$] (R^2=0.86), with a slope of 0.79 (Figure S2). That is, the reconstructed [PM] accounted for ~79% of the measured [$PM_{2.5}$]." (*Page 6 Line 155–157*)

In the revised supplement, Figure S2 shows:

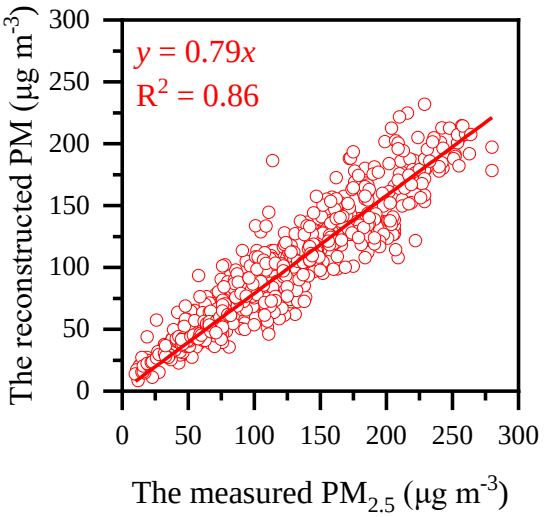

Figure S2. Linear relationship between the measured $PM_{2.5}$ concentration and the sum concentration of POA, LO-OOA, MO-OOA, NH_4NO_3, $(NH_4)_2SO_4$, BC and fine soil (the sum is referred to as the reconstructed PM).

The consequence of unaccounted mass of OA and ions in $PM_{1\text{-}2.5}$ on the calculated MSEs and MAEs are discussed and addressed in the comment (2).

Comment (2): The uncertainties of estimated MSEs and MAEs of chemical compositions in table 2 should be large due to the comment 1.

Response: Thank you for pointing this point. In this study, we measured OA and ions in PM_1 using Q-ACSM (method Sect. 2.2.2). However, a fraction of OA and ions can be distributed in $PM_{1\text{-}2.5}$, as the reviewer pointed out in the comment (1), which is not

considered in our analysis and thus will affect the calculation of the MSEs and MAEs following equations (2) and (3).

To address this concern, we conduct a sensitivity analysis with respect to the OA and ions mass concentrations. Their mass fraction in $PM_{1\text{-}2.5}$ is not known, and we use the fractional difference between the measured $PM_{2.5}$ and the reconstructed PM mass to represent it (i.e., 1−0.79=0.21). This value is in consistent with previous study in China (Sun et al., 2020). The analysis shows that if the OA and ions mass increased by 21% to include their mass in $PM_{1\text{-}2.5}$, the estimated MSEs and MAEs will correspondingly decrease by 21%. The moderate changes in mass concentrations of OA and ions will not significantly change any conclusions made in this study, because (1) both MSEs of NH_4NO_3, $(NH_4)_2SO_4$, POA, LO-OOA, MO-OOA, and MAEs of POA, LO-OOA, MO-OOA in Table 2 are overestimated by the similar extent, thus will not affect the comparison of MSEs and MAEs in Sect. 3.3; (2) the b_{ext} ($=b_{scat}+b_{abs}$) of chemical species, the product of the mass concentration and (MSEs+MAEs), does not change in the sensitivity analysis, compared with the results in Figure 4. The above sensitivity analysis has little effect on the MSEs of fine soil, because the fine soil is in $PM_{2.5}$ in this study (Sect. 2.2.2). The MAEs of BC is not affect, because it is also in $PM_{2.5}$ (Sect. 2.2.1); and is calculated by the independent absorption Angstrom exponent method (Sect. 2.4; Text S1).

In the revised manuscript, we add the following discussion in the main text:

> "The NH_4NO_3, $(NH_4)_2SO_4$, POA, LO-OOA, and MO-OOA in $PM_{1\text{-}2.5}$ are not included in the calculation (equations 2 and 3). A sensitivity analysis concludes that if their concentrations increased by 21% to match the measured $PM_{2.5}$, then the estimated MSEs and MAEs will correspondingly decrease by 21%." (*Page 6 Line 157–160*)

Comment (3): Generally, the formation mechanisms of NH_4NO_3 and $(NH_4)_2SO_4$ might be related with aqueous chemical processes. In Mie theory, their MSEs might be similar due to their similar size distributions. However, why their estimated MSEs are very different especially during the normal period?

Response: MSEs of NH_4NO_3 and $(NH_4)_2SO_4$ would be similar if they have similar particle diameters in Mie theory, considering that they have similar refraction indices and particle densities. However, we did not measure the particle size in this study campaign. Previous studies found different size distributions of NO_3^- and SO_4^{2-} measured in PM_1 in urban China in winter (Hu et al., 2017; Zhang et al., 2013; Zhu et al., 2021). Our previous study on the same campaign found that $(NH_4)_2SO_4$ was related with aqueous chemical processes, but NH_4NO_3 was also related with both aqueous chemical processes and photochemical oxidation (Tian et al., 2021). The different formation pathway of $(NH_4)_2SO_4$ and NH_4NO_3 could lead to their different size distributions. Therefore, the different MSEs of NH_4NO_3 and $(NH_4)_2SO_4$ were probably caused by their different size distributions. The differences in MSEs between NH_4NO_3 and $(NH_4)_2SO_4$ are larger during the normal period than those during the lockdown

period. However, we could not over-interpret this due to the lack of measured particle sizes.

To make this point clear, we add the following discussion in the revised manuscript:

> "NH_4NO_3 and $(NH_4)_2SO_4$ had different MSEs, probably due to their different size distributions (Hu et al., 2017; Zhang et al., 2013b; Zhu et al., 2021)." (*Page 9 Line 241–242*)

In the reference list, we add:

> "Hu, W., Hu, M., Hu, W. W., Zheng, J., Chen, C., Wu, Y. S., and Guo, S.: Seasonal variations in high time-resolved chemical compositions, sources, and evolution of atmospheric submicron aerosols in the megacity Beijing, Atmos. Chem. Phys., 17, 9979–10000, https://doi.org/10.5194/acp-17-9979-2017, 2017.
>
> Zhang, Y. M., Sun, J. Y., Zhang, X. Y., Shen, X. J., Wang, T. T., and Qin, M. K.: Seasonal characterization of components and size distributions for submicron aerosols in Beijing, Sci. China-Earth Sci., 56, 890–900, https://doi.org/10.1007/s11430-012-4515-z, 2013b.
>
> Zhu, W. F., Zhou, M., Cheng, Z., Yan, N. Q., Huang, C., Qiao, L. P., Wang, H. L., Liu, Y, C., Lou, S. R., and Guo, S.: Seasonal variation of aerosol compositions in Shanghai, China: Insights from particle aerosol mass spectrometer observations, Sci. Total Environ., 771, 144948, https://doi.org/10.1016/j.scitotenv.2021.144948, 2021."

Comment (4): (a) I suggest the author to further analyze the possible source or formation mechanisms of LO-OOA and MO-OOA. At least it needs to be discussed whether these OOAs came from the oxidation of POA or directly from the oxidation of VOCs. **(b)** According to the estimated MSEs of POA, LO-OOA and MO-OOA, mass median diameter of POA might be evidently lower than those of LO-OOA and MO-OOA. Why the MSEs of LO-OOA and MO-OOA is higher than that of POA needs further discussion. **(c)** In addition, why the MSE of MO-OOA during the lockdown period is higher than that during the normal period also needs further discussion.

Response: (a) In our previous study on the same campaign, we found that LO-OOA/ΔCO ratio was correlated well with both O_x (NO_2 + O_3) and aerosol liquid water content (ALWC). Same correlations were also found for MO-OOA. This indicates that both photochemical oxidation and aqueous-phase reaction were important pathways for the formation of LO-OOA and MO-OOA (Tian et al., 2021).

As the reviewer's comments, both the oxidation of POA and of VOCs contribute to the OOAs. In this study, OOAs are resolved using receptor models with mass-to-charge (*m/z*) fragments from 12 to 120 derived from measured OA data (method Sect. 2.2.2), identified by the mass spectra with high signal at *m/z* 44. Using this method, it is

challenging in distinguishing the contribution of POA and VOCs to OOAs formation (Canonaco et al., 2013).

(b) Previous studies found increased mass diameter of OA with increasing OA oxidation level (Wang et al., 2021; Xu et al., 2015). We agree with the reviewer that the MSEs increase from POA to MO-OOA could be attributed to their particle size growth. In the revised manuscript, to make it clear, we add:

> "The MSEs of OA increased with oxidation level from POA to MO-OOA. This could be explained by the increased mass diameter of OA with increasing OA oxidation level (Wang et al., 2021; Xu et al., 2015)." *(Page 9 Line 248–249)*

(c) In this study, the MSE of MO-OOA during the lockdown period was larger than that during the normal period. This is probably related to the enhanced atmospheric oxidation capacity during the lockdown period of this sampling campaign (Tian et al., 2021), which is also found in previous observations (Huang et al., 2020; Le et al., 2020). This results in the higher aging state of OA with larger diameter (Hu et al., 2016; Zhu et al., 2021), thus larger MSE during the lockdown period. We add this explanation to the revised Sect. 3.3:

> "The MSE of MO-OOA was larger during the lockdown period than that during the normal period, probably related to the enhanced atmospheric oxidation capacity during the lockdown period (Tian et al., 2021), which is found to result in higher aging state of OA with larger diameter (Hu et al., 2016; Zhu et al., 2021)." *(Page 9 Line 249–252)*

In the reference list, we add the new reference:

> "Hu, W. W., Hu, M., Hu, W., Jimenez, J. L., Yuan, B., Chen, W. T., Wang, M., Wu, Y. S., Chen, C., Wang, Z. B., Peng, J. F., Zeng, L. M., and Shao, M.: Chemical composition, sources, and aging process of submicron aerosols in Beijing: Contrast between summer and winter, J. Geophys. Res.-Atmos., 121, 1955–1977, https://doi.org/10.1002/2015JD024020, 2016."

Comment (5): The combined contribution of POA, LO-OOA and MO-OOA to b_{ext} was over 60% and the combined contribution of NH_4NO_3 and $(NH_4)_2SO_4$ was over 20% during the lockdown period in Fig. 4. In contrast, the contribution of biomass burning to b_{ext} was only 37% during the lockdown period in Fig. 6. This means that secondary organics and secondary inorganics from gaseous precursors (e.g., SO_2, NO_x and VOCs) emitted from coal combustion contributed slightly more to b_{ext} than biomass burning. Therefore, controlling biomass burning is as important as coal combustion in this city.

Response: We would like to stress that gaseous precursors (e.g., SO_2, NO_x and VOCs) are not solely from coal combustion, but also from biomass burning and vehicular emissions (Wang et al., 2017; Zhou et al., 2017). To our best knowledge, the receptor model method cannot quantify how much secondary organic and inorganic are from

gaseous precursors emitted from coal combustion. As shown in Figure 6, during the lockdown period, the contribution of secondary sources to b_{ext} (i.e., sulfate plus SOA source, 37.9%; nitrate plus SOA source, 11.8%) is larger than that of biomass burning (36.7%); however, we could not further attribute secondary sources to their respective primary source, e.g., coal combustion, biomass burning or vehicle emissions.

In this study, we make a conclusion that biomass burning is important to b_{ext} during the lockdown period, but not coal combustion, because (a) the contribution of biomass burning to b_{ext} (36.7%) is larger than coal combustion (6.7%), (b) the b_{ext} from biomass burning did not change significantly from normal to lockdown period, whereas the b_{ext} from coal combustion decreased by a factor of 2 from 73.6 ± 60.9 Mm^{-1} to 38.5 ± 34.5 Mm^{-1}. These changes are consistent with the control measures during the lockdown period, as stated in Sect. 3.4.

Comment (6): The contributions of six sources to DRE were estimated under the dry condition. To some extent, the contribution of coal combustion to b_{ext} might be significantly higher than that of biomass burning under ambient RH condition due to the hygroscopic growth according to comment 5.

Response: Yes, the contributions of six sources to DRE were estimated under the dry condition in this study, because atmospheric particles first pass through a Nafion® dryer before they were sampled by instruments (method Sect. 2.2.1).

As addressed in the comment (5), during the lockdown period the contribution of biomass burning to b_{ext} (36.7%) is much larger than that of coal combustion (6.7%). As shown in Figure 6, the b_{ext} from biomass burning was 215.4 ± 163.9 Mm^{-1}, 5 times higher than that from coal combustion (38.5 ± 34.5 Mm^{-1}) under dry condition. We agree with the reviewer that the b_{ext} under dry condition can be differ from the b_{ext} under ambient RH condition. To estimate the b_{ext} under ambient RH condition, we need to multiply the b_{ext} under dry condition by the f(RH) (i.e., hygroscopic growth factor). Under ambient RH condition, if coal combustion has higher b_{ext} than biomass burning, then the f(RH) of coal combustion should be at least 5 times higher than that of biomass burning, which is not very likely (Pitchford et al., 2007).

In this study, we focus on the contributions of different sources to b_{ext} and DRE. The influence of f(RH) on b_{ext} is beyond the scope of this manuscript. If the reviewer allows, we would prefer not to discuss it, to avoid distracting the readers, if possible. Because we tried to say that the contribution of biomass burning to b_{ext} and DRE is important during the lockdown period, and the influence of f(RH) on b_{ext} is not likely to change this conclusion.

References

Canonaco, F., Crippa, M., Slowik, J. G., Baltensperger, U., and Prévôt, A. S. H.: SoFi, an IGOR-based interface for the efficient use of the generalized multilinear engine (ME-2) for the source apportionment: ME-2 application to aerosol mass spectrometer data, Atmos. Meas. Tech., 6, 3649–3661, https://doi.org/10.5194/amt-6-3649-2013, 2013.

Hu, W., Hu, M., Hu, W. W., Zheng, J., Chen, C., Wu, Y. S., and Guo, S.: Seasonal variations in high time-resolved chemical compositions, sources, and evolution of atmospheric submicron aerosols in the megacity Beijing, Atmos. Chem. Phys., 17, 9979–10000, https://doi.org/10.5194/acp-17-9979-2017, 2017.

Hu, W. W., Hu, M., Hu, W., Jimenez, J. L., Yuan, B., Chen, W. T., Wang, M., Wu, Y. S., Chen, C., Wang, Z. B., Peng, J. F., Zeng, L. M., and Shao, M.: Chemical composition, sources, and aging process of submicron aerosols in Beijing: Contrast between summer and winter, J. Geophys. Res.-Atmos., 121, 1955–1977, https://doi.org/10.1002/2015JD024020, 2016.

Huang, X., Ding, A. J., Gao, J., Zheng, B., Zhou, D. R., Qi, X. M., Tang, R., Wang, J. P., Ren, C. H., Nie, W., Chi, X. G., Xu, Z., Chen, L. D., Li, Y. Y., Che, F., Pang, N. N., Wang, H. K., Tong, D., Qin, W., Cheng, W., Liu, W. J., Fu, Q. Y., Liu, B. X., Chai, F., Davis, J. S., Zhang, Q., and He, K. B.: Enhanced secondary pollution offset reduction of primary emissions during COVID-19 lockdown in China, Natl. Sci. Rev., 8, nwaa137, https://doi.org/10.1093/nsr/nwaa137, 2020.

Le, T. H., Wang, Y., Liu, L., Yang, J. N., Yung, Y., Li, G. H., and Seinfeld, J. H.: Unexpected air pollution with marked emission reductions during the COVID-19 outbreak in China, Science, 369, 702–706, https://doi.org/10.1126/science.abb7431, 2020.

Pitchford, M., Malm, W., Schichtel, B., Kumar, N., Lowenthal, D., and Hand, J.: Revised algorithm for estimating light extinction from IMPROVE particle speciation data, J. Air & Waste Manage. Assoc., 57, 1326–1336, https://doi.org/10.3155/1047-3289.57.11.1326, 2007.

Sun, Y. L., He, Y., Kuang, Y., Xu, W. Y., Song, S. J., Ma, N., Tao, J. C., Cheng, P., Wu, C., Su, H., Cheng, Y. F., Xie, C. H., Chen, C., Lei, L., Qiu, Y. M., Fu, P. Q., Croteau, P., and Worsnop, D. R.: Chemical differences between PM_1 and $PM_{2.5}$ in highly polluted environment and implications in air pollution studies, Geophys. Res. Lett., 47 (5), e2019GL086288, https://doi.org/10.1029/2019GL086288, 2020.

Tian, J., Wang, Q. Y., Zhang, Y., Yan, M. Y., Liu, H. K., Zhang, N. N., Ran, W. K., and Cao, J. J.: Impacts of primary emissions and secondary aerosol formation on air pollution in an urban area of China during the COVID-19 lockdown, Environ. Int., 150, 106426, https://doi.org/10.1016/j.evnint.2021.106426, 2021.

Wang, H. L., Jing, S. A., Lou, S. R., Hu, Q. Y., Li, L., Tao, S. K., Huang, C., Qiao, L. P., and Chen, C. H.: Volatile organic compounds (VOCs) source profiles of on-road vehicle emissions in China, Sci. Total Environ., 607–608, 253–261, https://doi.org/10.1016/j.scitotenv.2017.07.001, 2017.

Wang, J. F., Ye, J. H., Zhang, Q., Zhao, J., Wu, Y. Z., Li, J. Y., Liu, D. T., Li, W. J., Zhang, Y. G., Wu, C., Xie, C. H., Qin, Y. M., Lei, Y. L., Huang, X. P., Guo, J. P., Liu, P. F., Fu, P. Q., Li, Y. J., Lee, H. C., Choi, H., Zhang, J., Liao, H., Chen, M. D., Sun, Y. L., Ge, X. L., Martin, S. T., and Jacob, D. J.: Aqueous production of secondary organic aerosol from fossil-fuel emissions in winter Beijing haze, P.

Natl. Acad. Sci. USA., 118, e2022179118, https://doi.org/10.1073/pnas.2022179118, 2021.

Xu, W. Q., Sun, Y. L., Chen, C., Du, W., Han, T. T., Wang, Q. Q., Fu, P. Q., Wang, Z. F., Zhao, X. J., Zhou, L. B., Ji, D. S., Wang, P. C., and Worsnop, D. R.: Aerosol composition, oxidation properties, and sources in Beijing: results from the 2014 Asia-Pacific Economic Cooperation summit study, Atmos. Chem. Phys., 15, 13681–13698, https://doi.org/10.5194/acp-15-13681-2015, 2015.

Zhang, Y. M., Sun, J. Y., Zhang, X. Y., Shen, X. J., Wang, T. T., and Qin, M. K.: Seasonal characterization of components and size distributions for submicron aerosols in Beijing, Sci. China-Earth Sci., 56, 890–900, https://doi.org/10.1007/s11430-012-4515-z, 2013.

Zhou, Y., Xing, X. F., Lang, J. L., Chen, D. S., Cheng, S. Y., Wei, L., Wei, X., and Liu, C.: A comprehensive biomass burning emission inventory with high spatial and temporal resolution in China, Atmos. Chem. Phys., 17, 2839–2864, https://doi.org/10.5194/acp-17-2839-2017, 2017.

Zhu, W. F., Zhou, M., Cheng, Z., Yan, N. Q., Huang, C., Qiao, L. P., Wang, H. L., Liu, Y, C., Lou, S. R., and Guo, S.: Seasonal variation of aerosol compositions in Shanghai, China: Insights from particle aerosol mass spectrometer observations, Sci. Total Environ., 771, 144948, https://doi.org/10.1016/j.scitotenv.2021.144948, 2021.

Measurement report: The importance of biomass burning in light extinction and direct radiative effect of urban aerosol during the COVID-19 lockdown in Xi'an, China

Jie Tian[1,2], Qiyuan Wang[1,2,3], Huikun Liu[1], Yongyong Ma[4], Suixin Liu[1,2], Yong Zhang[1], Weikang Ran[1], Yongming Han[1,2,3], and Junji Cao[5]

[1]State Key Laboratory of Loess and Quaternary Geology, Institute of Earth Environment, Chinese Academy of Sciences, Xi'an 710061, China
[2]CAS Center for Excellence in Quaternary Science and Global Change, Xi'an 710061, China
[3]National Observation and Research Station of Regional Ecological Environment Change and Comprehensive Management in the Guanzhong Plain, Shaanxi, Xi'an 710061, China
[4]Meteorological Institute of Shaanxi Province, Xi'an 710015, China
[5]Institute of Atmospheric Physics, Chinese Academy of Sciences, Beijing 100029, China

Correspondence: Qiyuan Wang (wangqy@ieecas.cn) and Junji Cao (jjcao@mail.iap.ac.cn)

Abstract. Due to the complexity of emission sources, a better understanding of aerosol optical properties is required to mitigate climate change in China. Here, an intensive real-time measurement was conducted in an urban area of China before and during the lockdown of Coronavirus Disease 2019 (COVID-19), to explore the impacts of anthropogenic activities on aerosol light extinction and direct radiative effect (DRE). The mean light extinction coefficient (b_{ext}) reduced from 774.7 ±298.1 Mm^{-1} during the normal period to 544.3 ±179.4 Mm^{-1} during the lockdown period. The generalized additive model analysis indicated that the large decline of b_{ext} (29.7%) was attributed to the sharp reductions in anthropogenic emissions. Chemical calculation of b_{ext} based on the ridge regression analysis showed that organic aerosol (OA) was the largest contributor to b_{ext} in both periods (45.1–61.4%), and contributions of two oxygenated OAs to b_{ext} increased by 3.0–14.6% during the lockdown. A hybrid environmental receptor model combining with chemical and optical variables identified six sources of b_{ext}. It was found that b_{ext} from traffic-related emission, coal combustion, fugitive dust, nitrate plus secondary OA (SOA) source, and sulfate plus SOA source decreased by 21.4–97.9% in the lockdown, whereas b_{ext} from biomass burning increased by 27.1% mainly driven by undiminished needs of residential cooking and heating. The atmospheric radiative transfer model was further used to illustrate that biomass burning instead of traffic-related emission became the largest positive effect (10.0 ± 10.9 W m^{-2}) on aerosol DRE in the atmosphere during the lockdown. Our study provides insights into aerosol b_{ext} and DRE from anthropogenic sources, and the results implied the importance of controlling biomass burning for tackling climate change in China in the future.

1 Introduction

The abrupt outbreak of Coronavirus Disease 2019 (COVID-19) caused unprecedented economic and social disruption (Yao et al., 2020). Most worldwide countries implemented the city lockdown to curb the virus spread among humans, providing a rare opportunity to investigate the impacts of anthropogenic activities on the air quality (Ibrahim et al., 2021; Kumar et al., 2021; Sanap, 2021; Weber et al., 2020). The Chinese government also enforced a series of strict restrictions on travel, transport, manufacture, and constructive activities during the lockdown. Recent studies on the aerosols in China which were conducted during the lockdown period focused on primary emissions and secondary formation, and most of them had revealed changes in aerosol compositions, sources, and processes under a variety of emission control measures (Le et al., 2020; Li et al., 2020; Wang et al., 2020a; Wang et al., 2020c; Zhao et al., 2020; Zheng et al., 2020). However, only a few studies were conducted to explore the link of chemical constituents in aerosol with light absorption during the lockdown (Chen et al., 2020; Lin et al., 2021; Xu et al., 2020a). The influences of reduced anthropogenic activities on the variations of aerosol optical properties and direct radiative effect (DRE) are less understood.

Atmospheric aerosols alter the radiative energy budget by directly scattering and absorbing solar and terrestrial radiation to affect global climate change (Bellouin et al., 2013; Yao et al., 2017). The spatiotemporal variations of aerosol optical properties (e.g., light scattering coefficient (b_{scat}), light absorption coefficient (b_{abs}), light extinction coefficient (b_{ext}), and single scattering albedo (SSA)) highly depended on their chemical compositions and sources (Malm and Hand, 2007; Tao et al., 2014; Yao et al., 2021), can elevate uncertainties in estimating aerosol DRE (IPCC, 2013; Ma et al., 2012). Therefore, distinguishing chemical composition- and source-specific aerosol optical properties from a mixture of aerosols in the atmosphere would make a better understanding of the climate change during the COVID-19 lockdown.

The relationship between aerosol optical coefficients and chemical compositions can be built by the Interagency Monitoring of Protected Visual Environments algorithm and multiple linear regression (MLR) (Deng et al., 2016; Malm and Hand, 2007; Shen et al., 2014; Tao et al., 2014, 2015). However, previous studies often regarded organic aerosol (OA) as a whole light scattering component only. In reality, some OA components can absorb light, which is collectively termed as brown carbon (BrC) (Andreae and Gelencsér, 2006). The DRE caused by BrC has been reported to be nonnegligible (e.g., 0.04 W m^{-2} to 0.57 W m^{-2}) (Feng et al., 2013; Lin et al., 2014; Wang et al., 2014). Furthermore, the optical properties of OA can vary widely due to the complexity of OA components associated with primary sources, formation pathways, and aging processes (Laskin et al., 2015). For instance, primary OA (POA) from anthropogenic sources (e.g., biomass burning and coal combustion) usually has different mass scattering and absorption efficiencies (MSE and MAE) in the atmosphere compared to secondary OA (SOA) formed though photochemical or aqueous-phase oxidations (Han et al., 2015; Qin et al., 2018). Therefore, investigating POA and SOA contributions to aerosol light scattering and absorption would reduce uncertainties in the chemical apportionment of aerosol optical properties.

Previous studies have been conducted on the aerosol optical source apportionment. According to the multi-wavelength aethalometer measurement, the source of aerosol b_{abs} can be investigated by exploiting the differences in absorption spectra of light-absorbing materials (Herich et al., 2011; Sandradewi et al., 2008; Zotter et al., 2017). In this method, the aerosol absorption near-ultraviolet and short-visible regions of the spectrum from biomass burning are assumed to be enhanced because of BrC emitted, compared to that from fossil fuel combustion (Kirchstetter et al., 2004; Tian et al., 2019). This makes it possible to derive their contributions to light absorption by using the specific source absorption Ångström exponent (AAE), but the so-called "aethalometer model" could not distinguish as many sources resolved by receptor models due to the similar optical properties of the aerosol sources (Saarikoski et al., 2021). In contrast, receptor models can be utilized to resolve multiple optical source apportionment of aerosol. Several studies used a combination of the receptor model and MLR to indirectly identify sources of aerosol b_{scat}, b_{abs}, and b_{ext} (Cao et al., 2012; Tian et al., 2020; Zhou et al., 2017). For example, Zhou et al. (2017) firstly used positive matrix factorization analysis to quantify the mass contributions of aerosol from secondary aerosol, biomass burning, traffic-related emissions, and coal combustion based on the sole chemical species, and then the MLR was used to apportion the contribution of each source to b_{scat} and b_{abs}. In addition, recent studies have attempted to conduct direct optical source apportionment by combining aerosol chemical species with optical coefficients in one receptor model (Forello et al., 2019; Wang et al., 2020b; Xie et al., 2019). This promising method can provide both chemical and optical profiles in each source to improve the performance of source identification, and may eliminate potential uncertainties caused by the indirect approach.

The Fenwei Plain is designated as the key region of pollution treatment in the "Three-year action plan to fight air pollution" implemented by the Chinese State Council in 2018. As one of the megacities in this plain, Xi'an has been facing severe air pollution problem, especially in winter (Niu et al., 2016; Wang et al., 2015). Here, we conducted high time-resolved aerosol b_{scat} and b_{abs} measurements in Xi'an before and during the city lockdown in China. The main objectives are to (1) characterize the changes of aerosol optical properties since COVID-19 lockdown; (2) quantify the contributions of individual chemical composition and specific source to b_{ext}; and (3) evaluate source-specific aerosol DRE based on a radiative transfer model. This study provides insights into the response of aerosol b_{ext} and DRE to anthropogenic emission sources, which is a scientific basis for establishing future emission control policies to deal with climate change in China.

2 Methodology

2.1 Sampling site and period

Intensive measurements of aerosol optical properties were conducted at one urban sampling site of the National Observation and Research Station of Regional Ecological Environment Change and Comprehensive Management in the

Guanzhong Plain, southwest of Xi'an downtown (34°13' N, 108°52' E, Figure S1). All instruments were placed at the rooftop of an office building (~ 10 m above the ground) and approximately 30 m from the nearest traffic road. A detailed description of the sampling site can be found in Tian et al. (2021). In this study, the sampling campaign consisted of two distinct periods: normal period (January 1st to 23rd, 2020) and COVID-19 lockdown period (January 27th to February 7th, 2020). Three days of January 24th–26th, 2020 were excluded due to the intensive influence of fireworks for the Chinese New Year celebration.

2.2 Measurements

2.2.1 Real-time measurements of b_{scat} and b_{abs}

A single wavelength integrating nephelometer (Aurora 1000, Ecotech, Melbourne, Australia) was carried out to measure aerosol b_{scat} at a wavelength of 525 nm with a 5-min time resolution. In the measurement volume, the ambient air sampled with a flow rate of 5 L min^{-1} was illuminated by the light source, that only light scattered at scattering angles between 10 ° and 170 ° can reach the photomultiplier tube. Thereafter, b_{scat} can be calculated by the proportion of the electrical signals produced by the photomultiplier tube. Span calibration was made using CO_2 to ensure the accuracy of the instrument before sampling, and zero calibration was performed twice each day with particle-free air to subtract the Rayleigh scattering. More detailed principles of the Aurora 1000 have been described elsewhere (Chamberlain-Ward and Sharp, 2011).

Aerosol b_{abs} at wavelengths of 370 nm, 470 nm, 520 nm, 590 nm, 660 nm, and 880 nm were measured by a newly developed Aethalometer (model AE33, Magee Scientific, Berkeley, CA, USA) with a 1-min time resolution. Briefly, the model AE33 was the filter-based absorption photometer that simultaneously measured the light attenuation transmitted through two parallel spots of the aerosol filter with 3.85 L min^{-1} and 1.15 L min^{-1}, respectively. Based on "dual-spot" measurements, it used a real-time loading effect compensation algorithm to eliminate the nonlinear loading effect by increasing the deposition amount of aerosol on the filter. Additionally, a factor of 2.14 was used in the model AE33 to automatically modify the quartz filter matrix scattering effect. A detailed description of this instrument can be found in Drinovec et al. (2015).

Both of the Aurora 1000 and model AE33 instruments equipped with a $PM_{2.5}$ cyclone separator in the sampling inlet to remove particles larger than 2.5 μm, and a Nafion® dryer (MD-700-24S, Perma Pure, Inc., Lakewood, NJ, USA) to retain particles (relative humidity < 40%) before entering these instruments. Considering the relative error (1.5% ±0.1%) between b_{abs} at 520 nm and 525 nm is negligible, the amount of b_{ext} in this study was defined as the sum of b_{scat} at 525 nm and b_{abs} at 520 nm.

2.2.2 Complementary data

A quadrupole aerosol chemical speciation monitor (Q-ACSM, Aerodyne Research Inc., Billerica, Massachusetts, USA) and a Xact 625 ambient metals monitor (Xact 625i, Cooper Environmental Services, Beaverton, OR, USA) were operated to obtain chemical composition characteristics (Furger et al., 2020; Ng et al., 2011). The Q-ACSM measured concentrations of non-refractory species in PM_1 (NO_3^-, SO_4^{2-}, NH_4^+, Cl^-, and OA), and OA was further resolved into POA, less-, and more-oxidized oxygenated OA (LO-OOA and MO-OOA). Detailed information on the Q-ACSM data process and source apportionment of OA can be found in our previous paper (Tian et al., 2021). The Xact 625i quantified hourly element concentrations in $PM_{2.5}$ through X-ray fluorescence analysis, including Si, K, Ca, Cr, Mn, Fe, Zn, As, Se, Ba, Hg, and Pb. Additionally, BC concentration was calculated using b_{abs} at 880 nm (Kirchstetter et al., 2004). Online $PM_{2.5}$ and NO_x concentrations were obtained from the Department of Ecology and Environment of Shaanxi Province. More detailed descriptions of these complementary data can be found in Table S1.

2.3 Meteorological conditions separation

A generalized additive model (GAM) combined with integrated smoothness estimation was used to establish the relationship between b_{ext} and several meteorological parameters as follows (Wood, 2004):

$$\ln b_{ext}(i) = \sum_{j=1}^{7} f_j\left(\mathrm{MP}_j(i)\right) + \beta_0 + e_i \quad (1)$$

where $b_{ext}(i)$ is the b_{ext} in Mm^{-1} averaged over the i^{th} hour; MP_j represents the j^{th} meteorological parameter, such as wind speed, wind direction, temperature, pressure, dew point, and planetary boundary layer height, where the data sources can be found in Table S1; f corresponds to the smooth function describing the association between b_{ext} and meteorological parameters; β_0 is the model intercept; and e_i is the regression residuals which is assumed to be normally distributed.

Based on the R package "mgcv" (Wood, 2017), the whole campaign dataset was divided into three parts: a model data (80% of data during the normal period) for establishing the b_{ext} GAM, a test data (20% of data during the normal period) for verifying the accuracy of the model, and a forecast data (100% of data during the lockdown period) for estimating the contributions of meteorological conditions and emissions on b_{ext} reduction.

2.4 Chemical calculation of b_{scat} and b_{abs}

Because of POA and SOA with nonnegligible light scattering and absorbing abilities, the amount of b_{scat} and b_{abs} associated with individual chemical species can be estimated statistically using the ridge regression method:

$$b_{scat} = a_1[NH_4NO_3] + a_2[(NH_4)_2SO_4] + a_3[\text{fine soil}] + a_4[\text{POA}] + a_5[\text{LO-OOA}] + a_6[\text{MO-OOA}] + c_1 \quad (2)$$

$$b_{abs} = b_1[BC] + b_2[POA] + b_3[LO\text{-}OOA] + b_4[MO\text{-}OOA] + c_2 \quad (3)$$

where b_{scat} and b_{abs} are given in unit of Mm^{-1}; the bracket notation [] represents the specific chemical species concentration in μg m^{-3}; the a_i and b_i (i = 1–6) describe the MSE and MAE of each chemical species in the unit of m^2 g^{-1}, respectively; and c_i (i = 1 or 2) is the constant. In equation (2), the concentrations of [NH_4NO_3], [$(NH_4)_2SO_4$], and [fine soil] were calculated using 1.29 ×[NO_3^-], 1.35 ×[SO_4^{2-}], and [Fe]/0.032, respectively (Chow et al., 2015; CNEMC, 1990). In equation (3), b_1 was calculated by the absorption Ångström exponent method, and the detailed description can be seen in Text S1. The reconstructed [PM] ([PM] = [NH_4NO_3] + [$(NH_4)_2SO_4$] + [POA] + [LO-OOA] + [MO-OOA] + [BC] + [fine soil]) is strongly correlated with the measured [$PM_{2.5}$] (R^2 = 0.86), with a slope of 0.79 (Figure S2). That is, the reconstructed [PM] accounted for ~79% of the measured [$PM_{2.5}$]. The NH_4NO_3, $(NH_4)_2SO_4$, POA, LO-OOA, and MO-OOA in $PM_{1\text{-}2.5}$ are not included in the calculation (equations 2 and 3). A sensitivity analysis concludes that if their concentrations increased by 21% to match the measured $PM_{2.5}$, then the estimated MSEs and MAEs will correspondingly decrease by 21%.

2.5 Hybrid environmental receptor model (HERM) for source apportionment

The source apportionment of b_{ext} was performed with HERM which is a newly developed bilinear model (Chen and Cao, 2018). Briefly, the HERM solves non-negative matrices of unknown factor profiles and contributions with a pre-set number of factors K by iteratively minimizing the object function Q defined as follows:

$$Q = \sum_{j=1}^{J}\sum_{i=1}^{I} \frac{\left(x_{ij} - \sum_{k=1}^{K} g_{ik} f_{kj}\right)^2}{\sigma_{x_{ij}}^2 + \sum_{k=1}^{K}\left(g_{ik}^2 \sigma_{f_{kj}}^2 + \delta_{ik}\sigma_{x_{ij}}^2\right)} \quad (4)$$

where I, J, and K are the number of samples, aerosol variables, and factors, respectively; the indices of i, j, k represent the sample, aerosol variable, and factor, respectively; x_{ij} is the measured ambient data spectral matrix; f_{kj} is the factor profile matrix; g_{ik} is factor contribution matrix; $\sigma_{x_{ij}}$ and $\sigma_{f_{kj}}$ represent the error in measured ambient data and variability in constrained factor profile, respectively; δ_{ik} is set to 0 or 1 depending on whether the k^{th} factor profile is constrained or unconstrained, respectively.

In this study, both chemical species ($PM_{2.5}$, NO_3^-, SO_4^{2-}, NH_4^+, Cl^-, BC, POA, LO-OOA, MO-OOA, Si, K, Ca, Cr, Mn, Fe, Zn, As, Se, Ba, Hg, and Pb in μg m^{-3}) and optical variables (b_{scat} and b_{abs} in Mm^{-1}) were used as input data for the HERM analysis. The uncertainties of hourly ambient data except elements were introduced by the standard deviation of samples with higher time resolution (< 1-hour); the uncertainty of the element was estimated using its concentration, the default analytical relative error (10%) (Rai et al., 2020), and method detection limit (MDL) (Norris et al., 2014) (Text S2). All input variables were classified as strong due to the high signal-to-noise (SNR > 2). Here, the HERM had

predetermined: (1) the i^{th} sample was excluded from source apportionment when missing values occurred in variables; (2) $PM_{2.5}$ value in factor profile was set to unity as a reference standard for both chemical and optical variables.

A range of factor numbers from two to eight was selected to run in the HERM software with completely unconstrained factor profiles, and diagnostic plots are detailed in the supplementary material (Text S3 and Figures ~~S2~~S3–~~S7~~S8). The six-factor solution without mixed source was found to be the optimal solution based on multiple criteria including (1) variations in Q/Q_{exp} that can be used as a metric for choosing the best number of resolved factors (Ulbrich et al., 2009); (2) physical meaningfulness of distinct factor profiles and explained variations (EV) of variables; (3) agreement between the measured and modeled values; and (4) good correlations with external and internal tracers. Detailed information on the final selected factor profiles and contributions are presented in Section 3.4.

2.6 DRE calculations

The Santa Barbara DISORT Atmospheric Radiative Transfer (SBDART) developed by the Institute for Computational Earth System Science, University of California was utilized to estimate the source-specific aerosol DRE. It can calculate the downwelling and upwelling radiative flux (F_{down} and F_{up}), in which the difference indicates the net radiative flux ($\Delta F = F_{down} - F_{up}$). A detailed description of the SBDART can be found in Ricchiazzi et al. (1998). Based on the optical source apportionment results, the SBDART model input values of aerosol optical depth, SSA, asymmetry factor, and optical coefficients were retrieved using the Optical Properties of Aerosol and Cloud (OPAC) model (Hess et al., 1998). The aerosol DRE can be calculated as follows:

$$DRE_{atmosphere} = DRE_{top} - DRE_{surface} \quad (5)$$

$$DRE_{top} = \Delta F_{top}(\text{with aerosol}) - \Delta F_{top}(\text{without aerosol}) \quad (6)$$

$$DRE_{surface} = \Delta F_{surface}(\text{with aerosol}) - \Delta F_{surface}(\text{without aerosol}) \quad (7)$$

where the indices of atmosphere, top, and surface indicate the DRE in the atmosphere, at the top of the atmosphere, and the earth's surface, respectively; ΔF(with aerosol) and ΔF(without aerosol) represent the net radiative flux with and without aerosol, respectively.

3 Results and discussion

3.1 General descriptions of aerosol optical properties

The temporal variations of hourly mean b_{scat}, b_{abs}, b_{ext}, and SSA together with $PM_{2.5}$ mass concentrations for the entire sampling period are depicted in Figure 1, while a statistics summary of optical and chemical parameters during the

normal and COVID-19 lockdown periods is shown in Table 1. The optical coefficients decreased dramatically in accord with the significant reduction of $PM_{2.5}$ since stringent control measures on emission sources were implemented during the lockdown period (Tian et al., 2021; Zheng et al., 2020). The mean values of b_{scat}, b_{abs}, and b_{ext} during the normal period were 688.1 ±261.4 Mm^{-1}, 86.6 ±43.0 Mm^{-1}, and 774.7 ±298.1 Mm^{-1}, respectively, which are consistent with the values (657.4 ±436.9 Mm^{-1}, 104.0 ±69.6 Mm^{-1}, and 761.4 ±506.5 Mm^{-1}) reported previously in winter of 2009 in Xi'an (Cao et al., 2012), even though a series of nationwide air quality standards and long-term pollution control policies have been implemented in the 74 major cities since 2013 (Xu et al., 2020b; Zheng et al., 2018). Comparatively, the kind of control measures aiming to curb the outbreaks did not last long, but it was unprecedentedly strictest in China. The large decreases (27.6–47.0%) were found in b_{scat}, b_{abs}, and b_{ext} in the lockdown (498.4 ±159.0 Mm^{-1}, 45.9 ±22.9 Mm^{-1}, and 544.3 ± 179.4 Mm^{-1}, respectively), providing insights into the role of anthropogenic emissions on aerosol optical properties.

The SSA defined as the ratio of b_{scat} to b_{ext} increased from 0.89 ±0.03 during the normal period to 0.92 ±0.02 during the lockdown period. As presented in Figure 2a and b, SSA showed linear increases with the mass fractions of secondary inorganic aerosol (SIA = NH_4NO_3 + $(NH_4)_2SO_4$) to $PM_{2.5}$ (R^2 = 0.83–0.84) and SOA (SOA = LO-OOA + MO-OOA) to OA (R^2 = 0.94–0.99), indicating an enhanced role of secondary formation in the lockdown. In addition, the correlations of SSA and the ratio of LO-OOA to MO-OOA were established to reveal a more complex influence of SOA on SSA (Figure 2c), which showed negative relationships (R^2 = 0.69–0.79). It indicated that SSA can be impacted by the degree of oxidation on aerosol, and higher scattering and lower absorption abilities are usually found for more oxidized OA (Han et al., 2015; Lee et al., 2014).

3.2 Effects of emission reduction and meteorological conditions on reduced b_{ext}

Figure 3 shows the time series of the measured and GAM-predicted b_{ext} for the model data, test data, and forecast data. As shown in Tables S2 and S3, the constructed GAM with adjusted R^2 value (0.54) can explain 54% of the variation in b_{ext} after incorporating the nonlinear relationships between optical and meteorological parameters. Independent smoothed meteorological variables of the model were statistically significant by according to p values (< 0.05) from F test. Concurvity indices between each independent smoothed parameter were within 0.5, indicating there was no serious multicollinearity (Schimek, 2009).

Before applying the constructed GAM to predict the b_{ext} during the lockdown period, the cross-validation test was used to evaluate the model. For the test data (20% of data during the normal period), the R^2 value of the linear regression and index of agreement (IOA) (Wu et al., 2018) between the measured and GAM-predicted b_{ext} was 0.83 and 0.92, respectively, suggesting a good performance of the constructed GAM. The difference between the measured and GAM-

predicted b_{ext} in the lockdown can be attributed to emission reduction through the implementation of stringent control measures on emission sources. The emission reduction decreased b_{ext} by 299.2 Mm^{-1} during the lockdown period, higher than the decline of measured b_{ext} (230.4 Mm^{-1}) from normal to lockdown periods. It is indicated that the meteorological conditions enhanced b_{ext} by 68.8 Mm^{-1} during the lockdown period, further reflecting the effective control of anthropogenic emissions.

3.3 Contribution of chemical components to b_{ext}

Table 2 presents the estimated MSE and MAE of an individual chemical component during the normal and lockdown periods. NH_4NO_3 and $(NH_4)_2SO_4$ had different MSEs, probably due to their different size distributions (Hu et al., 2017; Zhang et al., 2013b; Zhu et al., 2021). The MSEs of NH_4NO_3 (3.74 ± 0.18 m^2 g^{-1}) and $(NH_4)_2SO_4$ (7.35 ± 0.25 m^2 g^{-1}) during the normal period were higher than those (3.23 ± 0.18 m^2 g^{-1} and 4.78 ± 0.35 m^2 g^{-1}) during the lockdown period. This may be explained by the higher mass loadings and peak diameters of aerosol without control measures (Cheng et al., 2015; Tao et al., 2015). The MAE of BC decreased from 15.00 m^2 g^{-1} to 13.27 m^2 g^{-1} related to the decline of AAE of BC (Text S1). The MSEs and MAEs of OA factors varied widely, from 3.48 m^2 g^{-1} to 12.89 m^2 g^{-1} and from 0.25 m^2 g^{-1} to 0.59 m^2 g^{-1}, respectively, due to the complex chemical variability of OA constituents (Hallquist et al., 2009; Moise et al., 2015). The MSEs of OA increased with oxidation level from POA to MO-OOA. This could be explained by the increased mass diameter of OA with increasing OA oxidation level (Wang et al., 2021; Xu et al., 2015). The MSE of MO-OOA was larger during the lockdown period than that during the normal period, probably related to the enhanced atmospheric oxidation capacity during the lockdown period (Tian et al., 2021), which is found to result in higher aging state of OA with larger diameter (Hu et al., 2016; Zhu et al., 2021).~~scattering ability of OA increased with oxidation level (from POA to MO-OOA) (Cappa et al., 2011; Flores et al., 2014); however,~~ The dependence on oxidation level of OA MAEs presented a more complex trend. LO-OOA had higher MAE values than those of POA, indicating more BrC chromophores with stronger light-absorbing capacity formed under less-oxidized condition (Zhang et al., 2020). Additionally, the effect of photo-bleaching in the atmosphere that can weaken the light absorption ability of BrC resulted in the reduction of MO-OOA MAEs (Wang et al., 2021).

The b_{ext} reconstructed by chemical compositions was strongly correlated with the measured optical b_{ext} (R^2 = 0.94), with a slope of 0.78~~Chemical calculation of b_{ext} was confirmed to be a reasonable estimation of aerosol optical coefficients by using chemical components data~~ (Figure~~s~~ ~~S8 and~~ S9). As shown in Figure 4, OA (POA + LO-OOA + MO-OOA) was the largest contributor to b_{ext} in both periods, accounting for 45.1–61.4%, followed by NH_4NO_3 (16.5–24.1%), BC (9.3–13.1%), $(NH_4)_2SO_4$ (7.9–11.2%), and fine soil (4.9–6.5%). This result was different from previous findings that SIA was often the largest contributor to b_{ext} in China, such as Beijing (46–54%) (Han et al., 2015), Chengdu (43%) (Tao et al., 2014), Nanjing (53%) (Shen et al., 2014), and Xi'an (63%) (Cao et al., 2012), highlighting the dominant role of organic

matters in aerosol light extinction in Xi'an today. Compared to the normal period, the contributions of NH_4NO_3, $(NH_4)_2SO_4$, fine soil, and BC, and POA to b_{ext} decreased by 1.3–7.6% in the lockdown, whereas contributions of two SOAs to b_{ext} increased by 3.0–14.6%. On the one hand, the mass concentrations of LO-OOA and MO-OOA decreased by 20.9–34.7% from normal to lockdown periods, lower than those of other chemical species (35.8–72.5%); On the other hand, both of SOAs MSEs and MAEs showed higher values during the lockdown period, especially MO-OOA. The combination of effects eventually led to an enhanced role of SOA in light extinction during the lockdown.

3.4 Contribution of sources to b_{ext}

The six-factor solution was selected to be the optimal solution, which can adequately account for the variability in $PM_{2.5}$ concentration and optical coefficients (Figures S10 and S11). Six sources were determined by the HERM analysis, consisting of traffic-related emission, biomass burning, coal combustion, fugitive dust, nitrate plus SOA source, and sulfate plus SOA source. Details about their characteristics are presented in Figure 5. The first source identified as traffic-related emission was characterized by high EV values of Cr (77%), Mn (53%), Fe (36%), and Zn (39%), which can be released from lubricating oils, fuel additives, and brake and tire wear (Ålander et al., 2005; Geivanidis et al., 2003; Tao et al., 2017; Zhang et al., 2013a). Moderate contributions of POA (26%) and BC (28%) were commonly regarded as species of diesel and gasoline engine exhaust (Chow et al., 2004; Liu et al., 2017). Additionally, the temporal variations in b_{ext} from this source correlated well with NO_x (R^2 = 0.72), suggesting an association with motor vehicle emissions (Huang et al., 2017; Li et al., 2017a). The second source with high EV values of POA (45%), LO-OOA (41%), BC (32%), Cl (34%), and K (41%) was judged to be biomass burning. K was regarded as an excellent tracer of biomass burning (Li et al., 2007; Ni et al., 2017), and good correlations were also found between b_{ext} from biomass burning and K (R^2 = 0.64). Previous studies have shown that POA from biomass burning can be rapidly oxidized in the atmosphere (Cubison et al., 2011), therefore, the abundant LO-OOA observed in this source might be indicative of aged biomass-burning aerosol (Crippa et al., 2013; Kim et al., 2017; Xu et al., 2015). The third source, coal combustion, was characterized by high EV values of Cl (42%), As (38%), Se (46%), and Pb (25%). Of these elements, As and Se were enriched in coals (Tian et al., 2013), which were reliable indicators for coal combustion (Tan et al., 2017; Yu et al., 2019); and Pb was found to possibly emitted from coal combustion in Xi'an (Xu et al., 2012). The fourth source was defined as fugitive dust due to significant EV values of Si (92%), Ca (63%), and Fe (31%), which were the dominant chemical species in natural and construction dust profiles (Liu et al., 2017; Zhao et al., 2006). Two secondary sources were resolved in our study as nitrate plus SOA source with high EV values of NO_3^- (42%), NH_4^+ (33%), and MO-OOA (34%) and sulfate plus SOA source with high EV values of SO_4^{2-} (58%) and MO-OOA (39%), respectively. Since SO_2 oxidation to sulfate needs a long time (e.g., 1 week) at the typical atmospheric level of OH radicals, SO_4^{2-} was likely associated with the regional source, while NO_3^- was often formed more locally due to the intense NO_x emissions in China

(Zhang et al., 2015; Zheng et al., 2014). The defined nitrate and sulfate plus SOA sources appeared to have stronger associations with local and regional processes, respectively.

As shown in Figure 6, the average b_{ext} from traffic-related emission, coal combustion and fugitive dust decreased from 77.3 ±46.8 Mm^{-1}, 73.6 ±60.9 Mm^{-1}, and 93.3 ±82.7 Mm^{-1} during the normal period to 1.7 ±4.0 Mm^{-1}, 38.5 ±34.5 Mm^{-1}, and 30.8 ±24.4 Mm^{-1} during the lockdown period, respectively, which can be explained by traffic restriction, closure of industries and stopping construction activities. b_{ext} from traffic-related emission with the largest reduction (97.9%) emphasized the effectiveness of controlling private gasoline cars and commercial and construction diesel trucks in the lockdown (Wang et al., 2020c). For two secondary sources, though previous studies reported the enhancement of secondary aerosol formation efficiencies as the increase of atmospheric oxidation capacity in the lockdown (Huang et al., 2020; Le et al., 2020; Tian et al., 2021), the decreases in gas and organic precursors (e.g., NO_2, SO_2, and VOCs) led to the 47.5% and 21.4% reductions of b_{ext} from sources of nitrate plus SOA and sulfate plus SOA, respectively. That is, the enhanced secondary aerosol cannot offset the primary emission reduction in Xi'an, confirming that reducing anthropogenic primary emissions is still the most effective treatment of aerosol pollution.

By contrast, the average b_{ext} from biomass burning during the lockdown period (215.4 ±163.9 Mm^{-1}) was higher than that during the normal period (169.4 ± 196.9 Mm^{-1}). The government didn't strengthen the past control policies that forbade biomass burning in the lockdown. Moreover, strict controls were enforced on the movements of people, even in the countryside, possibly resulting more consumption of biomass for cooking and heating. As shown in Figure 7, the rising stages of $PM_{2.5}$ during the lockdown period were all accompanied by the increase in b_{ext} from biomass burning, accounting for 46.4–55.6% of the total b_{ext}. Take the rising stage of $PM_{2.5}$ from 13:00 30 to 7:00 31 January as an example, b_{ext} from POA and LO-OOA increased rapidly at rates of 8.6 Mm^{-1} $hour^{-1}$ and 8.2 Mm^{-1} $hour^{-1}$, respectively. Correspondingly, b_{ext} from biomass burning showed the fastest rise (26.0 Mm^{-1} $hour^{-1}$) in all primary sources, which led to biomass burning becoming the most important source to b_{ext} (36.7%) in the lockdown (Figure 6). Hence, additional actions and investigations on biomass burning emissions would be taken into consideration.

3.5 Impacts of COVID-19 lockdown on aerosol DRE

Figure 8 shows the range of source-specific aerosol DRE_{top}, $DRE_{surface}$, and $DRE_{atmosphere}$ during the normal and lockdown periods. For all sources, the aerosol $DRE_{atmosphere}$ values in both periods were positive, producing net warming effects in the atmosphere. The mean aerosol $DRE_{atmosphere}$ decreased from 31.0 ±23.2 W m^{-2} before the lockdown to 14.1 ±11.5 W m^{-2} in the lockdown, with a reduction of 54.5%. This can be explained by the reduced aerosol concentration and increased SSA (Liu et al., 2020).

With regard to the contributions of specific sources on the $DRE_{atmosphere}$, traffic-related emission had the largest positive effect on $DRE_{atmosphere}$ during the normal period, with the value of 13.3 ± 9.2 W m^{-2}, followed by biomass burning (8.4 ± 13.0 W m^{-2}), coal combustion (7.8 ± 7.2 W m^{-2}), sulfate plus SOA source (1.7 ± 3.0 W m^{-2}), and fugitive dust (1.1 ± 2.4 W m^{-2}). Nitrate and plus SOA source presented the negative value of $DRE_{atmosphere}$ (-1.2 ± 0.7 W m^{-2}), suggesting the cooling effect in the atmosphere. Due to the strictest traffic restrictions implemented, the $DRE_{atmosphere}$ from traffic-related emission (0.4 ± 1.0 W m^{-2}) showed a significant reduction (97.0%) in the lockdown. However, the $DRE_{atmosphere}$ from biomass burning increased to 10.0 ± 10.9 W m^{-2}, indicating that biomass burning was not effectively controlled during the lockdown period. The other four sources contributed relatively small amounts of $DRE_{atmosphere}$; that is 4.5 ± 4.5 W m^{-2} for coal combustion, -0.3 ± 0.8 W m^{-2} for fugitive dust, -1.4 ± 0.8 W m^{-2} for nitrate plus SOA source, and 1.0 ± 1.8 W m^{-2} for sulfate plus SOA source. Similar to Xi'an city, the pollution sources of traffic and biomass burning were the two most significant anthropogenic sources of aerosol in most Chinese cities, such as Chengdu, Guangzhou, Jinan, Tianjin, and etc (Cheng et al., 2021; Huang et al., 2018; Khan et al., 2021; Li et al., 2017b). The results in this study indicated that the control measures on traffic in the lockdown were highly effective for mitigating the effects of climate change in the short term, while future emission control policies should consider the importance of biomass burning to tackle climate change in China.

4 Conclusion

This study conducted an intensive real-time measurement campaign in an urban city of China before and during the lockdown of Coronavirus Disease 2019 to investigate the impacts of anthropogenic emissions on aerosol optical properties and direct radiative effect (DRE). Decreases in light scattering coefficient (b_{scat}), light absorption coefficient (b_{abs}), and light extinction coefficient (b_{ext}) were observed in the lockdown with reductions of 27.6–47.0%, in accord with the decline of $PM_{2.5}$ under strict emission control measures. Single scattering albedo during the lockdown period (0.92 ± 0.02) was higher than that during the normal period (0.89 ± 0.03), suggesting an enhanced role of secondary formation in the lockdown. The generalized additive model analysis showed that meteorological conditions enhanced b_{ext} by 68.8 Mm^{-1} during the lockdown period, thus, the dramatical reduction of b_{ext} was credited to anthropogenic emission reductions.

The relationship between b_{ext} and chemical components was established based on the ridge regression analysis. Using the estimated mass scattering and absorption efficiencies (MSEs and MAEs) of chemical components, OA including primary OA, less-, and more-oxidized oxygenated OA was found to be the largest contributor (45.1–61.4%) to b_{ext} before and during the lockdown period, followed by NH_4NO_3 (16.5–24.1%), BC (9.3–13.1%), $(NH_4)_2SO_4$ (7.9–11.2%), and

fine soil (4.9–6.5%). Particularly, secondary OA played an increasingly important part in light extinction during the lockdown when contributions of two oxygenated OAs to b_{ext} increased by 3.0–14.6%.

A hybrid environmental receptor model coupled with chemical and optical variables was utilized to carry out optical source apportionment. Six sources of b_{ext} were resolved, including traffic-related emission, biomass burning, coal combustion, fugitive dust, nitrate plus SOA source, and sulfate plus SOA source. Most sources showed reductions of b_{ext} (21.4–97.9%) during the lockdown, confirming the effectiveness of reducing anthropogenic primary emissions for treating aerosol pollution. b_{ext} from traffic-related emission had the most evident decrement (97.9%), whereas that from biomass burning increased by 27.1% during the lockdown due to the undiminished needs of residential cooking and heating in winter.

The atmospheric radiative transfer further illustrated that aerosol produced net warming effects (14.1–31.0 W m^{-2}) in the atmosphere during the normal and lockdown periods. Biomass burning instead of traffic-related emission became the largest positive effect (10.0 ± 10.9 W m^{-2}) on aerosol DRE in the atmosphere in the lockdown. The results implied that reducing biomass burning would be another direct and effective way of climate change mitigation besides traffic restriction, therefore, the Chinese government should further tighten the policy on controlling biomass burning in the future.

Data availability. Data used to support the findings in this study are archived at the Institute of Earth Environment, Chinese Academy of Sciences, and are publicly available at https://doi.org/10.5281/zenodo.6457841~~5993130~~.

Competing interests. The authors declare that they have no conflict of interest.

Author contributions. QW, YH, and JC designed the campaign. SL, YZ, and WR conducted field measurements. JT, HL, and YM made data analysis and interpretation. JT wrote the paper with contributions from all co-authors.

Acknowledgments. The authors are grateful to the staff from the National Observation and Research Station of Regional Ecological Environment Change and Comprehensive Management in the Guanzhong Plain, Shaanxi for their assistance with field sampling.

Financial support. This research was jointly supported by the Key Research and Development Program of Shaanxi Province (grant no. 2018-ZDXM3-01), the Strategic Priority Research Program of Chinese Academy of Sciences (grant no. XDB40000000), the West Light Foundation of the Chinese Academy of Sciences (grant no. XAB2019B05), the Sino-Swiss Cooperation on Air Pollution Source Apportionment for Better Air (grant no. 7F-09802.01.02), and the Youth Innovation Promotion Association of the Chinese Academy of Sciences (grant no. 2019402).

References

Ålander, T., Antikainen, E., Raunemaa, T., Elonen, E., Rautiola, A., and Torkkell, K.: Particle emissions from a small two-stroke engine: Effects of fuel, lubricating oil, and exhaust aftertreatment on particle characteristics, Aerosol Sci. Tech., 39, 151–161, https://doi.org/1 0.1080/027868290910224, 2005.

Andreae, M. O. and Gelencsér, A.: Black carbon or brown carbon? The nature of light-absorbing carbonaceous aerosols, Atmos. Chem. Phys., 6, 3131–3148, https://doi.org/10.5194/acp-6-3131-2006, 2006.

Bellouin, N., Quaas, J., Morcrette, J. J., and Boucher, O.: Estimates of aerosol radiative forcing from the MACC re-analysis, Atmos. Chem. Phys., 13, 2045–2062, https://doi.org/10.5194/acp-13-2045-2013, 2013.

Cao, J. J., Wang, Q. Y., Chow, J. C., Watson, J. G., Tie, X. X., Shen, Z. X., Wang, P., and An, Z. S.: Impacts of aerosol compositions on visibility impairment in Xi'an, China, Atmos. Environ., 59, 559–566, https://doi.org/10.1016/j.atmosenv.2012.05.036, 2012.

Cappa, C. D., Che, D. L., Kessler, S. H., Kroll, J. H., and Wilson, K. R.: Variations in organic aerosol optical and hygroscopic properties upon heterogeneous OH oxidation, J. Geophys. Res. Atmos., 116, D15204, https://doi.org/10.1029/2011JD015918, 2011.

Chamberlain-Ward, S. and Sharp, F.: Advances in Nephelometry through the Ecotech Aurora Nephelometer, The Scientific World Journal, 11, 2530–2535, https://doi.org/10.1100/2011/310769, 2011.

Chen, L. W. and Cao, J.: $PM_{2.5}$ source apportionment using a Hybrid Environmental Receptor Model, Environ. Sci. Technol., 52, 6357–6369, https://doi.org/10.1021/acs.est.8b00131, 2018.

Chen, Y., Zhang, S. M., Peng, C., Shi, G. M., Tian, M., Huang, R. J., Guo, D. M., Wang, H. B., Yao, X. J., and Yang, F. M.: Impact of the COVID-19 pandemic and control measures on air quality and aerosol light absorption in southwestern China, Sci. Total Environ., 749, 141419, https://doi.org/10.1016/j.scitotenv.2020.141419, 2020.

Cheng, M. T., Tang, G. Q., Lv, B., Li, X. R., Wu, X. R., Wang, Y. M., and Wang, Y. S.: Source apportionment of $PM_{2.5}$ and visibility in Jinan, China, J. Environ. Sci., 102, 207–215, https://doi.org/10.1016/j.jes.2020.09.012, 2021.

Cheng, Z., Jiang, J. K., Chen, C. H., Gao, J., Wang, S. X., Watson, J. G., Wang, H. L., Deng, J. G., Wang, B. Y., Zhou, M., Chow, J. C., Pitchford, M. L., and Hao, J. M.: Estimation of aerosol mass scattering efficiencies under high mass loading: Case study for the megacity of Shanghai, China, Environ. Sci. Technol., 49, 831–838, https://doi.org/10.1021/es504567q, 2015.

China National Environmental Monitoring Centre (CNEMC).: Background values of soil elements in China, Chinese Environmental Press, Beijing (in Chinese), 1990.

Chow, J. C., Lowenthal, D. H., Chen, L. W. A., Wang, X. L., and Watson, J. G.: Mass reconstruction methods for $PM_{2.5}$: a review, Air Qual. Atmos. Health, 8, 243–263, https://doi.org/10.1007/s11869-015-0338-3, 2015.

Chow, J. C., Watson, J. G., Kuhns, H., Etyemezian, V., Lowenthal, D. H., Crow, D., Kohl, S. D., Engelbrecht, J. P., and Green, M. C.: Source profiles for industrial, mobile, and area sources in the Big Bend Regional Aerosol Visibility and Observational study, Chemosphere, 54, 185–208, https://doi.org/10.1016/j.chemosphere.2003.07.004, 2004.

Crippa, M., DeCarlo, P. F., Slowik, J. G., Mohr, C., Heringa, M. F., Chirico, R., Poulain, L., Freutel, F., Sciare, J., Cozic, J., Di Marco, C. F., Elsasser, M., Nicolas, J. B., Marchand, N., Abidi, E., Wiedensohler, A., Drewnick, F., Schneider, J., Borrmann, S., Nemitz, E., Zimmermann, R., Jaffrezo, J. L., Prévôt, A. S. H., and Baltensperger, U.: Wintertime aerosol chemical composition and source apportionment of the organic fraction in the metropolitan area of Paris, Atmos. Chem. Phys., 13, 961–981, https://doi.org/10.5194/acp-13-961-2013, 2013.

Cubison, M. J., Ortega, A. M., Hayes, P. L., Farmer, D. K., Day, D., Lechner, M. J., Brune, W. H., Apel, E., Diskin, G. S., Fisher, J. A., Hecobian, A., Knapp, D. J., Mikoviny, T., Riemer, D., Sachse, G. W., Sessions, W., Weber, R. J., Weinheimer, A. J., and Jimenez, J. L.: Effects of aging on organic aerosol from open biomass burning smoke in aircraft and lab studies, Atmos. Chem. Phys., 11, 12049–12064, https://doi.org/10.5194/acpd-11-12103-2011, 2011.

Deng, J. J., Zhang, Y. R., Hong, Y. W., Xu, L. L., Chen, Y. T., Du, W. J., and Chen, J. S.: Optical properties of $PM_{2.5}$ and the impacts of chemical compositions in the coastal city Xiamen in China, Sci. Total Environ., 557–558, 665–675, https://doi.org/10.1016/j.scitotenv.2016.03.143, 2016.

Drinovec, L., Močnik, G., Zotter, P., Prévôt, A. S. H., Ruckstuhl, C., Coz, E., Rupakheti, M., Sciare, J., Müller, T., Wiedensohler, A., and Hansen, A. D. A.: The "dual-spot" Aethalometer: an improved measurement of aerosol black carbon with real-time loading compensation, Atmos. Meas. Tech., 8, 1965–1979, https://doi.org/10.5194/amt-8-1965-2015, 2015.

Feng, Y., Ramanathan, V., and Kotamarthi, V. R.: Brown carbon: a significant atmospheric absorber of solar radiation? Atmos. Chem. Phys., 13, 8607–8621, https://doi.org/10.5194/acp-13-8607-2013, 2013.

~~Flores, J. M., Zhao, D. F., Segev, L., Schlag, P., Kiendler-Scharr, A., Fuchs, H., Watne, A. K., Bluvshtein, N., Mentel, T. F., and Hallquist, M.: Evolution of the complex refractive index in the UV spectral region in ageing secondary organic aerosol, Atmos. Chem. Phys., 14, 5793–5806, https://doi.org/10.5194/acp-14-5793-2014, 2014.~~

Forello, A. C., Bernardoni, V., Calzolai, G., Lucarelli, F., Massabò, D., Nava, S., Pileci, R. E., Prati, P., Valentini, S., Valli, G., and Vecchi, R.: Exploiting multi-wavelength aerosol absorption coefficients in a multi-time resolution source apportionment study to retrieve source-dependent absorption parameters, Atmos. Chem. Phys., 19, 11235–11252, https://doi.org/10.5194/acp-19-11235-2019, 2019.

Furger, M., Rai, P., Slowik, J. G., Cao, J. J., Visser, S., Baltensperger, U., and Prévôt, A. S. H.: Automated alternating sampling of PM_{10} and $PM_{2.5}$ with an online XRF spectrometer, Atmos. Environ.: X, 5, 100065, https://doi.org/10.1016/j.aeaoa.2020.100065, 2020.

Geivanidis, S., Pistikopoulos, P., and Samaras, Z.: Effect on exhaust emissions by the use of methylcyclopentadienyl manganese tricarbonyl (MMT) fuel additive and other lead replacement gasolines, Sci. Total Environ., 305, 129–141, https://doi.org/10.1016/S0048-9697(02)00476-X, 2003.

Hallquist, M., Wenger, J. C., Baltensperger, U., Rudich, Y., Simpson, D., Claeys, M., Dommen, J., Donahue, N. M., George, C., Goldstein, A. H., Hamilton, J. F., Herrmann, H., Hoffmann, T., Iinuma, Y., Jang, M., Jenkin, M. E., Jimenez, J. L., Kiendler-Scharr, A., Maenhaut, W., McFiggans, G., Mentel, Th. F., Monod, A., Prévôt, A. S. H., Seinfeld, J. H., Surratt, J. D., Szmigielski, R., and Wildt, J.: The formation, properties and impact of secondary organic aerosol: current and emerging issues, Atmos. Chem. Phys., 9, 5155–5236, https://doi.org/10.5194/acp-9-5155-2009, 2009.

Han, T. T., Xu, W. Q., Chen, C., Liu, X. G., Wang, Q. Q., Li, J., Zhao, X. J., Du, W., Wang, Z. F., and Sun, Y. L.: Chemical apportionment of aerosol optical properties during the Asia-Pacific Economic Cooperation summit in Beijing, China, J. Geophys. Res.-Atmos., 120, 12281–12295, https://doi.org/10.1002/2015JD023918, 2015.

Herich, H., Hueglin, C., and Buchmann, B.: A 2.5 year's source apportionment study of black carbon from wood burning and fossil fuel combustion at urban and rural sites in Switzerland, Atmos. Meas. Tech., 4, 1409–1420, https://doi.org/10.5194/amt-4-1409-2011, 2011.

Hess, M., Koepke, P., and Schult, I.: Optical properties of aerosols and clouds: The software package OPAC, B. Am. Meteorol. Soc., 79, 831–844, https://doi.org/10.1175/1520-0477(1998)079<0831:OPOAAC>2.0.CO;2, 1998.

Hu, W., Hu, M., Hu, W. W., Zheng, J., Chen, C., Wu, Y. S., and Guo, S.: Seasonal variations in high time-resolved chemical compositions, sources, and evolution of atmospheric submicron aerosols in the megacity Beijing, Atmos. Chem. Phys., 17, 9979–10000, https://doi.org/10.5194/acp-17-9979-2017, 2017.

Hu, W. W., Hu, M., Hu, W., Jimenez, J. L., Yuan, B., Chen, W. T., Wang, M., Wu, Y. S., Chen, C., Wang, Z. B., Peng, J. F., Zeng, L. M., and Shao, M.: Chemical composition, sources, and aging process of submicron aerosols in Beijing:

Contrast between summer and winter, J. Geophys. Res.-Atmos., 121, 1955–1977, https://doi.org/10.1002/2015JD024020, 2016.

Huang, X., Ding, A. J., Gao, J., Zheng, B., Zhou, D. R., Qi, X. M., Tang, R., Wang, J. P., Ren, C. H., Nie, W., Chi, X. G., Xu, Z., Chen, L. D., Li, Y. Y., Che, F., Pang, N. N., Wang, H. K., Tong, D., Qin, W., Cheng, W., Liu, W. J., Fu, Q. Y., Liu, B. X., Chai, F., Davis, J. S., Zhang, Q., and He, K. B.: Enhanced secondary pollution offset reduction of primary emissions during COVID-19 lockdown in China, Natl. Sci. Rev., 8, nwaa137, https://doi.org/10.1093/nsr/nwaa137, 2020.

Huang, X. F., Zou, B. B., He, L. Y., Hu, M., Prévôt, A. S. H., and Zhang, Y. H.: Exploration of $PM_{2.5}$ sources on the regional scale in the Pearl River Delta based on ME-2 modeling, Atmos. Chem. Phys., 18, 11563–11580, https://doi.org/10.5194/acp-18-11563-2018, 2018.

Huang, X. J., Liu, Z. R., Liu, J. Y., Hu, B., Wen, T. X., Tang, G. Q., Zhang, J. K., Wu, F. K., Ji, D. S., Wang, L. L., and Wang, Y. S.: Chemical characterization and source identification of $PM_{2.5}$ at multiple sites in the Beijing-Tianjin-Hebei region, China, Atmos. Chem. Phys., 17, 12941–12962, https://doi.org/10.5194/acp-17-12941-2017, 2017.

Ibrahim, S., Landa, M., Pešek, O., Pavelka, K., and Halounova, L.: Space-time machine learning models to analyze COVID-19 pandemic lockdown effects on aerosol optical depth over Europe, Remote Sens., 13, 3027, https://doi.org/10.3390/rs13153027, 2021.

IPCC: Climate change 2013: The physical science basis. Contribution of working group I to the fifth assessment reprot of the intergovemental panel on climate change [Stocker, T. F., D. Qin, G. -K. Plattner, M. Tignor, S. K. Allen, J. Boschung, A. Nauels, Y. Xia, V. Bex and P.M. Midgley (eds.)]. Cambridage University Press, Cambrigde, United Kingdom and New York, NY, USA, 1535pp, 2013.

Khan, J. Z., Sun, L., Tian, Y. Z., Shi, G. L., and Feng, Y. C.: Chemical characterization and source apportionment of PM_1 and $PM_{2.5}$ in Tianjin, China: Impacts of biomass burning and primary biogenic sources, J. Environ. Sci., 99, 196–209, https://doi.org/10.1016/j.jes.2020.06.027, 2021.

Kim, H., Zhang, Q., Bae, G. N., Kim, J. Y., and Lee, S. B.: Sources and atmospheric processing of winter aerosols in Seoul, Korea: Insights from real-Time measurements using a high-resolution aerosol mass spectrometer, Atmos. Chem. Phys., 17, 2009–2033, https://doi.org/10.5194/acp-17-2009-2017, 2017.

Kirchstetter, T.W., Novakov, T., and Hobbs, P. V.: Evidence that the spectral dependence of light absorption by aerosols is affected by organic carbon, J. Geophys. Res.-Atmos., 109, D21208, doi:10.1029/2004JD004999, 2004.

Kumar, D., Singh, A. K., Kumar, V., Poyoja, R., Ghosh, A., and Singh, B.: COVID-19 driven changes in the air quality; a study of major cities in the Indian state of Uttar Pradesh, Environ. Pollut., 274, 116512, https://doi.org/10.1016/j.envpol.2021.116512, 2021.

Laskin, A., Laskin, J., and Nizkorodov, S. A.: Chemistry of atmospheric brown carbon, Chem. Rev., 115, 10, 4335–4382, https://doi.org/10.1021/cr5006167, 2015.

Le, T. H., Wang, Y., Liu, L., Yang, J. N., Yung, Y., Li, G. H., and Seinfeld, J. H.: Unexpected air pollution with marked emission reductions during the COVID-19 outbreak in China, Science, 369, 702–706, https://doi.org/10.1126/science.abb7431, 2020.

Lee, H. J., Aiona, P. K., Laskin, A., Laskin, J., and Nizkorodov, S. A.: Effect of solar radiation on the optical properties and molecular composition of laboratory proxies of atmospheric brown carbon, Environ. Sci. Technol., 48, 10217–10226, https://doi.org/10.1021/es502515r, 2014.

Li, H. Y., Zhang, Q., Zhang, Q., Chen, C. R., Wang, L. T., Wei, Z., Zhou, S., Parworth, C., Zheng, B., Canonaco, F., Prévôt, A. S. H., Chen, P., Zhang, H. L., Wallington, T. J., and He, K. B.: Wintertime aerosol chemistry and haze

evolution in an extremely polluted city of the North China Plain: significant contribution from coal and biomass combustion, Atmos. Chem. Phys., 17, 4751–4768, https://doi.org/10.5194/acp-17-4751-2017, 2017a.

Li, L., Li, Q., Huang, L., Wang, Q., Zhu, A. S., Xu, J., Liu, Z. Y., Li, H. L., Shi, L. S., Li, R., Azari, M., Wang, Y. J., Zhang, X. J., Liu, Z. Q., Zhu, Y. H., Zhang, K., Xue, S. H., Ooi, M. C. G., Zhang, D. P., and Chan, A.: Air quality changes during the COVID-19 lockdown over the Yangtze River Delta Region: An insight into the impact of human activity pattern changes on air pollution variation, Sci. Total Environ., 732, 139282, https://doi.org/10.1016/j.scitotenv.2020.139282, 2020.

Li, L. L, Tan, Q. W., Zhang, Y. H., Feng, M., Qu, Y., An, J. L., and Liu, X. G.: Characteristics and source apportionment of $PM_{2.5}$ during persistent extreme haze events in Chengdu, southwest China, Environ. Pollut., 230, 718–729, https://doi.org/10.1016/j.envpol.2017.07.029, 2017b.

Li, X. H., Wang, S. X., Duan, L., Hao, J. M., Li, C., Chen, Y. S., and Yang, L.: Particulate and trace gas emissions from open burning of wheat straw and corn stover in China, Environ. Sci. Technol., 41, 6052–6058, https://doi.org/10.1021/es0705137, 2007.

Lin, G. X., Penner, J. E., Flanner, M. G., Sillman, S., Xu, L., and Zhou, C.: Radiative forcing of organic aerosol in the atmosphere and on snow: Effects of SOA and brown carbon, J. Geophys. Res.-Atmos., 119, 7453–7476, https://doi.org/10.1002/2013JD021186, 2014.

Lin, Y. C., Zhang, Y. L., Xie, F., Fan, M. Y., and Liu, X.: Substantial decreases of light absorption, concentrations and relative contributions of fossil fuel to light-absorbing carbonaceous aerosols attributed to the COVID-19 lockdown in east China, Environ. Pollut., 275, 116615, https://doi.org/10.1016/j.envpol.2021.116615, 2021.

Liu, B. S., Wu, J. H., Zhang, J. Y., Wang, L., Yang, J. M., Liang, D. N., Dai, Q. L., Bi, X. H., Feng, Y. C., Zhang, Y. F., and Zhang, Q. X.: Characterization and source apportionment of $PM_{2.5}$ based on error estimation from EPA PMF 5.0 model at a medium city in China, Environ. Pollut., 222, 10–22, https://doi.org/10.1016/j.envpol.2017.01.005, 2017.

Liu, D. T., Hu, K., Zhao, D. L., Ding, S., Wu, Y. F., Zhou, C., Yu, C. J., Tian, P., Liu, Q., Bi, K., Wu, Y. Z., Hu, B., Ji, D. S., Kong, S. F., Ouyang, B., He, H., Huang, M. Y., and Ding, D. P.: Efficient vertical transport of black carbon in the planetary boundary layer, Geophys. Res. Lett., 47, e2020GL088858, https://doi.org/10.1029/2020GL088858, 2020.

Ma, X., Yu, F., and Luo, G.: Aerosol direct radiative forcing based on GEOS-Chem-APM and uncertainties, Atmos. Chem. Phys., 12, 5563–5581, https://doi.org/10.5194/acp-12-5563-2012, 2012.

Malm, W. C. and Hand, J. L.: An examination of the physical and optical properties of aerosols collected in the IMPROVE program, Atmos. Environ., 41, 3407–3427, https://doi.org/10.1016/j.atmosenv.2006.12.012, 2007.

Moise, T., Flores, J. M., and Rudich, Y.: Optical properties of secondary organic aerosols and their changes by chemical processes, Chem. Rev., 115, 4400–4439, https://doi.org/10.1021/cr5005259, 2015.

Ng, N. L., Herndon, S. C., Trimborn, A., Canagaratna, M. R., Croteau, P. L., Onasch, T. B., Sueper, D., Worsnop, D. R., Zhang, Q., Sun, Y. L., and Jayne, J. T.: An aerosol chemical speciation monitor (ACSM) for routine monitoring of the composition and mass concentrations of ambient aerosol, Aerosol Sci. Technol., 45, 780–794, https://doi.org/10.1080/02786826.2011.560211, 2011.

Ni, H. Y., Tian, J., Wang, X. L., Wang, Q. Y., Han, Y. M., Cao, J. J., Long, X., Chen, L.-W. A., Chow, J. C., and Watson, J. G.: $PM_{2.5}$ emissions and source profiles from open burning of crop residues, Atmos. Environ., 169, 229–237, https://doi.org/10.1016/j.atmosenv.2017.08.063, 2017.

Niu, X. Y., Cao, J. J., Shen, Z. X., Ho, S. S. H., Tie, X. X., Zhao, S. Y., Xu, H. M., Zhang, T., and Huang, R. J.: $PM_{2.5}$ from the Guanzhong Plain: Chemical composition and implications for emission reductions, Atmos. Environ., 147, 458–469, https://doi.org/10.1016/j.atmosenv.2016.10.029, 2016.

Norris, G., Duvall, R., Brown, S., and Bai, S.: EPA positive matrix factorization (PMF) 5.0 fundamentals and user guide, 2014.

Qin, Y. M., Tan, H. B., Li, Y. J., Li, Z. J., Schurman, M. I., Liu, L., Wu, C., and Chan, C. K.: Chemical characteristics of brown carbon in atmospheric particles at a suburban site near Guangzhou, China, Atmos. Chem. Phys., 18, 16409–16418, https://doi.org/10.5194/acp-18-16409-2018, 2018.

Rai, P., Furger, M., Slowik, J. G., Canonaco, F., Fröhlich, R., Hüglin, C., Minguillón, M. C., Petterson, K., Baltensperger, U., and Prévôt, A. S. H.: Source apportionment of highly time-resolved elements during a firework episode from a rural freeway site in Switzerland, Atmos. Chem. Phys., 20, 1657–1674, https://doi.org/10.5194/acp-20-1657-2020, 2020.

Ricchiazzi, P., Yang, S. R., Gautier, C., and Sowle, D.: SBDART: A research and teaching software tool for Plane-parallel radiative transfer in the Earth's atmosphere, B. Am. Meteorol. Soc., 79, 2101–2114, https://doi.org/10.1175/1520-0477(1998)079<2101:SARATS>2.0.CO;2, 1998.

Saarikoski, S., Niemi, J. V., Aurela, M., Pirjola, L., Kousa, A., Rönkkö, T., and Timonen, H.: Sources of black carbon at residential and traffic environments obtained by two source apportionment methods, Atmos. Chem. Phys., 21, 14851–14869, https://doi.org/10.5194/acp-21-14851-2021, 2021.

Sanap, S. D.: Global and regional variations in aerosol loading during COVID-19 imposed lockdown, Atmos. Environ., 246, 118132, https://doi.org/10.1016/j.atmosenv.2020.118132, 2021.

Sandradewi, J., Prévôt, A. S. H., Szidat, S., Perron, N., Alfarra, M. R., Lanz, V. A., Weingartner, E., and Baltensperger, U.: Using aerosol light absorption measurements for the quantitative determination of wood burning and traffic emission contributions to particulate matter, Environ. Sci. Technol., 42, 3316–3323, https://doi.org/10.1021/es702253m, 2008.

Schimek, M. G.: Semiparametric penalized generalized additive models for environmental research and epidemiology, Environmetrics, 20, 699–717, https://doi.org/10.1002/env.972, 2009.

Shen, G. F., Xue, M., Yuan, S. Y., Zhang, J., Zhao, Q. Y., Li, B., Wu, H. S., and Ding, A. J.: Chemical compositions and reconstructed light extinction coefficients of particulate matter in a mega-city in the western Yangtze River Delta, China, Atmos. Environ., 83, 14–20, https://doi.org/10.1016/j.atmosenv.2013.10.055, 2014.

Tan, J. H., Zhang, L. M., Zhou, X. M., Duan, J. C., Li, Y., Hu, J. N., and He, K. B.: Chemical characteristics and source apportionment of $PM_{2.5}$ in Lanzhou, China, Sci. Total Environ., 601–602, 1743–1752, https://doi.org/10.1016/j.scitotenv.2017.06.050, 2017.

Tao, J., Zhang, L. M., Cao, J. J., Zhong, L. J., Chen, D. S., Yang, Y. H., Chen, D. H., Chen, L. G., Zhang, Z. S., Wu, Y., Xia, Y. J., Ye, S. Q., and Zhang, R. J.: Source apportionment of $PM_{2.5}$ at urban and suburban areas of the Pearl River Delta region, south China - With emphasis on ship emissions, Sci. Total Environ., 574, 1559–1570, https://doi.org/10.1016/j.scitotenv.2016.08.175, 2017.

Tao, J., Zhang, L. M., Cao, J., Hsu, S. C., Xia, X. G., Zhang, Z. S., Lin, Z. J., Cheng, T. T., and Zhang, R. J.: Characterization and source apportionment of aerosol light extinction in Chengdu, southwest China, Atmos. Environ., 95, 552–562, https://doi.org/10.1016/j.atmosenv.2014.07.017, 2014.

Tao, J., Zhang, L. M., Gao, J., Wang, H., Chai, F. H., and Wang, S. L: Aerosol chemical composition and light scattering during a winter season in Beijing, Atmos. Environ., 110, 36–44, https://doi.org/10.1016/j.atmosenv.2015.03.037, 2015.

Tian, H. Z., Lu, L., Hao, J. M., Gao, J. J., Cheng, K., Liu, K. Y., Qiu, P. P., and Zhu, C. Y.: A review of key hazardous trace elements in Chinese coals: Abundance, occurrence, behavior during coal combustion and their environmental impacts, Energ. Fuel., 27, 601–614, https://doi.org/10.1021/ef3017305, 2013.

Tian, J., Wang, Q. Y., Han, Y. M., Ye, J. H., Wang, P., Pongpiachan, S., Ni, H. Y., Zhou, Y. Q., Wang, M., Zhao, Y. Z., and Cao, J. J.: Contributions of aerosol composition and sources to particulate optical properties in a southern coastal city of China, Atmos. Res., 235, 104744, https://doi.org/ 10.1016/j.atmosres.2019.104744, 2020.

Tian, J., Wang, Q. Y., Ni, H. Y., Wang, M., Zhou, Y. Q., Han, Y. M., Shen, Z. X., Pongpiachan, S., Zhang, N. N., Zhao, Z. Z., Zhang, Q., Zhang, Y., Long, X., and Cao, J. J.: Emission characteristics of primary brown carbon absorption from biomass and coal burning: Development of an optical emission inventory for China, J. Geophys. Res.-Atmos., 124, 1879–1893, https://doi.org/10.1029/2018JD029352, 2019.

Tian, J., Wang, Q. Y., Zhang, Y., Yan, M. Y., Liu, H. K., Zhang, N. N., Ran, W. K., and Cao, J. J.: Impacts of primary emissions and secondary aerosol formation on air pollution in an urban area of China during the COVID-19 lockdown, Environ. Int., 150, 106426, https://doi.org/10.1016/j.envint.2021.106426, 2021.

Ulbrich, I. M., Canagaratna, M. R., Zhang, Q., Worsnop, D. R., and Jimenez, J. L.: Interpretation of organic components from Positive Matrix Factorization of aerosol mass spectrometric data, Atmos. Chem. Phys., 9, 2891–2918, https://doi.org/10.5194/acp-9-2891-2009, 2009.

Wang, J. F., Ye, J. H., Zhang, Q., Zhao, J., Wu, Y. Z., Li, J. Y., Liu, D. T., Li, W. J., Zhang, Y. G., Wu, C., Xie, C. H., Qin, Y. M., Lei, Y. L., Huang, X. P., Guo, J. P., Liu, P. F., Fu, P. Q., Li, Y. J., Lee, H. C., Choi, H., Zhang, J., Liao, H., Chen, M. D., Sun, Y. L., Ge, X. L., Martin, S. T., and Jacob, D. J.: Aqueous production of secondary organic aerosol from fossil-fuel emissions in winter Beijing haze, P. Natl. Acad. Sci. USA., 118, e2022179118, https://doi.org/10.1073/pnas.2022179118, 2021.

Wang, P., Cao, J. J., Shen, Z. X., Han, Y. M., Lee, S. C., Huang, Y., Zhu, C. S., Wang, Q. Y., Xu, H. M., and Huang, R. J.: Spatial and seasonal variations of $PM_{2.5}$ mass and species during 2010 in Xi'an, China, Sci. Total Environ., 508, 477–487, https://doi.org/10.1016/j.scitotenv.2014.11.007, 2015.

Wang, P.F., Chen, K.Y., Zhu, S.Q., Wang, P., and Zhang, H.L.: Severe air pollution events not avoided by reduced anthropogenic activities during COVID-19 outbreak, Resour. Conserv. Recycl., 158, 104814, https://doi.org/10.1016/j.resconrec.2020.104814, 2020a.

Wang, Q. Y., Liu, H. K., Wang, P., Dai, W. T., Zhang, T., Zhao, Y. Z., Tian, J., Zhang, W. Y., Han, Y. M., and Cao, J. J.: Optical source apportionment and radiative effect of light-absorbing carbonaceous aerosols in a tropical marine monsoon climate zone: the importance of ship emissions, Atmos. Chem. Phys., 20, 15537–15549, https://doi.org/10.5194/acp-20-15537-2020, 2020b.

Wang, X., Heald, C. L., Ridley, D. A., Schwarz, J. P., Spackman, J. R., Perring, A. E., Coe, H., Liu, D., and Clarke, A. D.: Exploiting simultaneous observational constraints on mass and absorption to estimate the global direct radiative forcing of black carbon and brown carbon, Atmos. Chem. Phys., 14, 17527–17583, https://doi.org/10.5194/acp-14-10989-2014, 2014.

Wang, Y. C., Yuan, Y., Wang, Q. Y., Liu, C. G., Zhi, Q., and Cao, J. J.: Changes in air quality related to the control of coronavirus in China: Implications for traffic and industrial emissions, Sci. Total Environ., 731, 139133, https://doi.org/10.1016/j.scitotenv.2020.139133, 2020c.

Weber, J., Shin, Y. M., Staunton Sykes, J., Archer-Nicholls, S., Abraham, N. L., and Archibald, A. T.: Minimal climate impacts from short-lived climate forcers following emission reductions related to the COVID-19 pandemic, Geophys. Res. Lett., 47, e2020GL090326. https://doi.org/10.1029/2020GL090326, 2020.

Wood, S. N.: Generalized additive models: An introduction with R (2nd ed), CRC press, 496pp, https://doi.org/10.1201/9781315370279, 2017.

Wood, S. N.: Stable and efficient multiple smoothing parameter estimation for generalized additive models, J. Am. Stat. Assoc., 99, 673–686, https://doi.org/10.1198/016214504000000980, 2004.

Wu, J. R., Bei, N. F., Li, X., Cao, J. J., Feng, T., Wang, Y. C., Tie, X. X., and Li, G. H.: Widespread air pollutants of the North China Plain during the Asian summer monsoon season: a case study, Atmos. Chem. Phys., 18, 8491–8504, https://doi.org/10.5194/acp-18-8491-2018, 2018.

Xie, M. J., Chen, X., Holder, A. L., Hays, M. D., Lewandowski, M., Offenberg, J. H., Kleindienst, T. E., Jaoui, M., and Hannigan, M. P.: Light absorption of organic carbon and its sources at a southeastern U.S. location in summer, Environ. Pollut., 244, 38–46, https://doi.org/10.1016/j.envpol.2018.09.125, 2019.

Xu, H. M., Cao, J. J., Ho, K. F., Ding, H., Han, Y. M., Wang, G. H., Chow, J. C., Watson, J. G., Khol, S. D., Qiang, J., Li, W. T.: Lead concentrations in fine particulate matter after the phasing out of leaded gasoline in Xi'an, China, Atmos. Environ., 46, 217–224, https://doi.org/10.1016/j.atmosenv.2011.09.078, 2012.

Xu, L., Zhang, J., Sun, X., Xu, S. C., Shan, M., Yuan, Q., Liu, L., Du, Z. H., Liu, D. T., Xu, D., Song, C. B., Liu, B. W., Lu, G. D., Shi, Z. B., and Li, W. J.: Variation in concentration and sources of black carbon in a megacity of China during the COVID-19 pandemic, Geophys. Res. Lett., 47, e2020GL090444, https://doi.org/10.1029/2020GL090444, 2020a.

Xu, W. Q., Sun, Y. L., Chen, C., Du, W., Han, T. T., Wang, Q. Q., Fu, P. Q., Wang, Z. F., Zhao, X. J., Zhou, L. B., Ji, D. S., Wang, P. C., and Worsnop, D. R.: Aerosol composition, oxidation properties, and sources in Beijing: results from the 2014 Asia-Pacific Economic Cooperation summit study, Atmos. Chem. Phys., 15, 13681–13698, https://doi.org/10.5194/acp-15-13681-2015, 2015.

Xu, W. Y., Kuang, Y., Bian, Y. X., Liu, L., Li, F., Wang, Y. Q., Xue, B., Luo, B., Huang, S., Yuan, B., Zhao, P. S., and Shao, M.: Current challenges in visibility improvement in southern China, Environ. Sci. Technol. Lett., 7, 395–401, https://doi.org/10.1021/acs.estlett.0c00274, 2020b.

Yao, H., Song, Y., Liu, M. X., Archer-Nicholls, S., Lowe, D., McFiggans, G., Xu, T. T., Du, P., Li, J. F., Wu, Y. S., Hu, M., Zhao, C., and Zhu, T.: Direct radiative effect of carbonaceous aerosols from crop residue burning during the summer harvest season in East China, Atmos. Chem. Phys., 17, 5205–5219, https://doi.org/10.5194/acp-17-5205-2017, 2017.

Yao, L. Q., Kong, S. F., Zheng, H., Chen, N., Zhu, B., Xu, K., Cao, W. X., Zhang, Y., Zheng, M. M., Cheng, Y., Hu, Y., Zhang, Z. X., Yan, Y. Y., Liu, D. T., Zhao, T. L., Bai, Y. Q., and Qi, S. H.: Co-benefits of reducing $PM_{2.5}$ and improving visibility by COVID-19 lockdown in Wuhan, NPJ Clim. Atmos. Sci., 4, 40, https://doi.org/10.1038/s41612-021-00195-6, 2021.

Yao, M. S., Zhang, L., Ma, J. X., and Zhou, L.: On airborne transmission and control of SARS-Cov-2, Sci. Total Environ., 731, 139178, https://doi.org/10.1016/j.scitotenv.2020.139178, 2020.

Yu, Y. Y., He, S. Y., Wu, X. L., Zhang, C., Yao, Y., Liao, H., Wang, Q. G., and Xie, M. J.: $PM_{2.5}$ elements at an urban site in Yangtze River Delta, China: High time-resolved measurement and the application in source apportionment, Environ. Pollut., 253, 1089–1099, https://doi.org/10.1016/j.envpol.2019.07.096, 2019.

Zhang, R., Jing, J., Tao, J., Hsu, S. C., Wang, G., Cao, J., Lee, C. S. L., Zhu, L., Chen, Z., Zhao, Y., and Shen, Z.: Chemical characterization and source apportionment of $PM_{2.5}$ in Beijing: seasonal perspective, Atmos. Chem. Phys., 13, 7053–7074, https://doi.org/10.5194/acp-13-7053-2013, 2013a.

Zhang, R. Y., Wang, G. H., Guo, S., Zamora, M. L., Ying, Q., Lin, Y., Wang, W. G., Hu, M., and Wang, Y.: Formation of urban fine particulate matter, Chem. Rev., 115, 3803–3855, https://doi.org/10.1021/acs.chemrev.5b00067, 2015.

Zhang, Q., Shen, Z. X., Zhang, L. M., Zeng, Y. L., Ning, Z., Zhang, T., Lei, Y. L., Wang, Q. Y., Li, G. H., Sun, J., Westerdahl, D., Xu, H. M., and Cao, J. J.: Investigation of primary and secondary particulate brown carbon in two Chinese cities of Xi'an and Hong Kong in wintertime, Environ. Sci. Technol., 54, 3803 – 3813, https://doi.org/10.1021/acs.est.9b05332, 2020.

Zhang, Y. M., Sun, J. Y., Zhang, X. Y., Shen, X. J., Wang, T. T., and Qin, M. K.: Seasonal characterization of components and size distributions for submicron aerosols in Beijing, Sci. China-Earth Sci., 56, 890–900, https://doi.org/10.1007/s11430-012-4515-z, 2013b.

Zhao, P. S., Feng, Y. C., Tan, Z., and Wu, J. H.: Characterizations of resuspended dust in six cities of North China, Atmos. Environ., 40, 5807–5814, https://doi.org/10.1016/j.atmosenv.2006.05.026, 2006.

Zhao, Y. B., Zhang, K., Xu, X. T., Shen, H. Z., Zhu, X., Zhang, Y. X., Hu, Y. T., and Shen, G. F.: Substantial changes in nitrogen dioxide and ozone after excluding meteorological impacts during the COVID-19 outbreak in mainland China, Environ. Sci. Technol. Lett., 7, 402–408, https://doi.org/10.1021/acs.estlett.0c00304, 2020.

Zheng, B., Huo, H., Zhang, Q., Yao, Z. L., Wang, X. T., Yang, X. F., Liu, H., and He, K. B.: High-resolution mapping of vehicle emissions in China in 2008, Atmos. Chem. Phys., 14, 9787–9805, https://doi.org/10.5194/acp-14-9787-2014, 2014.

Zheng, B., Tong, D., Li, M., Liu, F., Hong, C. P., Geng, G. N., Li, H. Y., Li, X., Peng, L. Q., Qi, J., Yan, L., Zhang, Y. X., Zhao, H. Y., Zheng, Y. X., He, K. B., and Zhang, Q.: Trends in China's anthropogenic emissions since 2010 as the consequence of clean air actions, Atmos. Chem. Phys., 18, 14095–14111, https://doi.org/10.5194/acp-18-14095-2018, 2018.

Zheng, H., Kong, S. F., Chen, N., Yan, Y. Y., Liu, D. T., Zhu, B., Xu, K., Cao, W. X., Ding, Q. Q., Lan, B., Zhang, Z. X., Zheng, M. M., Fan, Z. W., Cheng, Y., Zheng, S. R., Yao, L. Q., Bai, Y. Q., Zhao, T. L., and Qi, S. H.: Significant changes in the chemical compositions and sources of $PM_{2.5}$ in Wuhan since the city lockdown as COVID-19. Sci. Total Environ., 739, 140000, https://doi.org/10.1016/j.scitotenv.2020.140000, 2020.

Zhou, Y. Q., Wang, Q. Y., Huang, R. J., Liu, S. X., Tie, X. X., Su, X. L., Niu, X. Y., Zhao, Z. Z., Ni, H. Y., Wang, M., Zhang, Y. G., and Cao, J. J.: Optical properties of aerosols and implications for radiative effects in Beijing during the Asia-Pacific Economic Cooperation (APEC) Summit 2014, J. Geophys. Res.-Atmos., 122, 10119–10132, https://doi.org/10.1002/2017jd026997, 2017.

Zhu, W. F., Zhou, M., Cheng, Z., Yan, N. Q., Huang, C., Qiao, L. P., Wang, H. L., Liu, Y, C., Lou, S. R., and Guo, S.: Seasonal variation of aerosol compositions in Shanghai, China: Insights from particle aerosol mass spectrometer observations, Sci. Total Environ., 771, 144948, https://doi.org/10.1016/j.scitotenv.2021.144948, 2021.

Zotter, P., Herich, H., Gysel, M., El-Haddad, I., Zhang, Y., Močnik, G., Hüglin, C. Baltensperger, U., Szidat, S., and Prévôt, A. S. H.: Evaluation of the absorption Ångström exponents for traffic and wood burning in the Aethalometer-based source apportionment using radiocarbon measurements of ambient aerosol, Atmos. Chem. Phys., 17, 4229–4249, https://doi.org/10.5194/acp-17-4229-2017, 2017.

Table 1. Summary of optical coefficients and chemical species in Xi'an observed in the entire campaign, normal period (January 1st to 23rd, 2020), and COVID-19 lockdown period (January 27th to February 7th, 2020).

Parameters*	Entire campaign	Normal period	COVID-19 lockdown period	Change ratio**
Optical coefficients				
b_{scat}	623.2 ± 248.3	688.1 ± 261.4	498.4 ± 159.0	27.6%
b_{abs}	72.6 ± 42.1	86.6 ± 43.0	45.9 ± 22.9	47.0%
b_{ext}	695.8 ± 285.3	774.7 ± 298.1	544.3 ± 179.4	29.7%
SSA	0.90 ± 0.03	0.89 ± 0.03	0.92 ± 0.02	-3.2%
Chemical species				
$PM_{2.5}$	116.4 ± 56.3	134.4 ± 56.9	81.8 ± 34.9	39.1%
NH_4NO_3	33.1 ± 17.3	40.2 ± 16.4	19.5 ± 8.8	51.6%
$(NH4)_2SO_4$	8.3 ± 4.6	9.5 ± 4.9	5.9 ± 2.5	38.1%
fine soil	11.8 ± 8.0	15.8 ± 7.2	4.3 ± 1.9	72.5%
BC	4.4 ± 2.6	5.4 ± 2.6	2.7 ± 1.3	50.6%
POA	18.3 ± 12.4	20.9 ± 12.7	13.4 ± 10.1	35.8%
LO-OOA	7.6 ± 5.8	8.6 ± 6.4	5.6 ± 3.7	34.7%
MO-OOA	11.1 ± 4.5	12.0 ± 4.8	9.5 ± 3.3	20.9%

*The units for b_{scat}, b_{abs}, b_{ext} are Mm^{-1}; SSA is dimensionless; The units of chemical species are $\mu g\ m^{-3}$.

**Change ratio = ([Normal period] − [COVID-19 lockdown period])/[Normal period]×100%.

Table 2. Estimated MSEs and MAEs (m^2 g^{-1}) of individual chemical components during normal and COVID-19 lockdown periods.

Components	Normal period		COVID-19 lockdown period	
	MSE	MAE	MSE	MAE
NH_4NO_3	3.74 ± 0.18		3.23 ± 0.18	
$(NH_4)_2SO_4$	7.35 ± 0.25		4.78 ± 0.35	
fine soil	2.46 ± 0.35		3.39 ± 0.79	
BC		15.00		13.27
POA	3.90 ± 0.18	0.25 ± 0.01	3.48 ± 0.16	0.29 ± 0.01
LO-OOA	8.62 ± 0.27	0.27 ± 0.02	9.87 ± 0.35	0.59 ± 0.03
MO-OOA	9.87 ± 0.45	/	12.89 ± 0.55	0.31 ± 0.04

*MAE of MO-OOA during the normal period was negative (near zero) and not listed in the table.

715

Figure captions:

Figure 1. Hourly variations of light scattering (b_{scat}), absorption (b_{abs}), and extinction (b_{ext}) coefficients, single scattering albedo (SSA), and $PM_{2.5}$ mass concentrations in Xi'an during the normal (January 1st to 23rd, 2020) and COVID-19 lockdown (January 27th to February 7th, 2020) periods.

Figure 2. Variations of single scattering albedo (SSA) as a function of (a) secondary inorganic aerosol (SIA = NH_4NO_3 + $(NH_4)_2SO_4$)/$PM_{2.5}$, (b) secondary organic aerosol (SOA = LO-OOA + MO-OOA)/OA, and (c) LO-OOA/MO-OOA ratios during the normal and COVID-19 lockdown periods.

Figure 3. Time series of the measured and GAM-predicted light extinction coefficient (b_{ext}) for the model data, test data, and forecast data.

Figure 4. Contributions of NH_4NO_3, $(NH_4)_2SO_4$, fine soil, BC, POA, LO-OOA, and MO-OOA to the reconstructed chemical light extinction coefficient (b_{ext}) during the normal and COVID-19 lockdown periods.

Figure 5. (a) Profiles and (b) time series plots of the resolved source factors in the six-factor solution, including traffic-related emission, biomass burning, coal combustion, fugitive dust, nitrate plus SOA source, and sulfate plus SOA source. The columns in each factor are the profile that displays the relative relation of absolute values of variables. The red dot represents the explained variation of species for different factors. The corresponding time trends of chemical tracers are also shown.

Figure 6. Contributions of six resolved sources to the modeled source light extinction coefficient (b_{ext}) during the normal and COVID-19 lockdown periods, including traffic-related emission, biomass burning, coal combustion, fugitive dust, nitrate plus SOA source, and sulfate plus SOA source.

Figure 7. Time series of $PM_{2.5}$ mass concentration, the light extinction coefficient (b_{ext}) of chemical species, and the b_{ext} from six resolved sources during the lockdown period. Pie charts depicting the average fractional contributions of chemical species and sources to b_{ext} during the $PM_{2.5}$ rising stages, which were marked in light gray.

Figure 8. Direct radiative effect (DRE) of aerosol from traffic-related emission, biomass burning, coal combustion, fugitive dust, nitrate plus SOA source, and sulfate plus SOA source at the earth's surface, the top of the atmosphere, and in the atmosphere during the normal (a) and COVID-19 lockdown (b) periods.

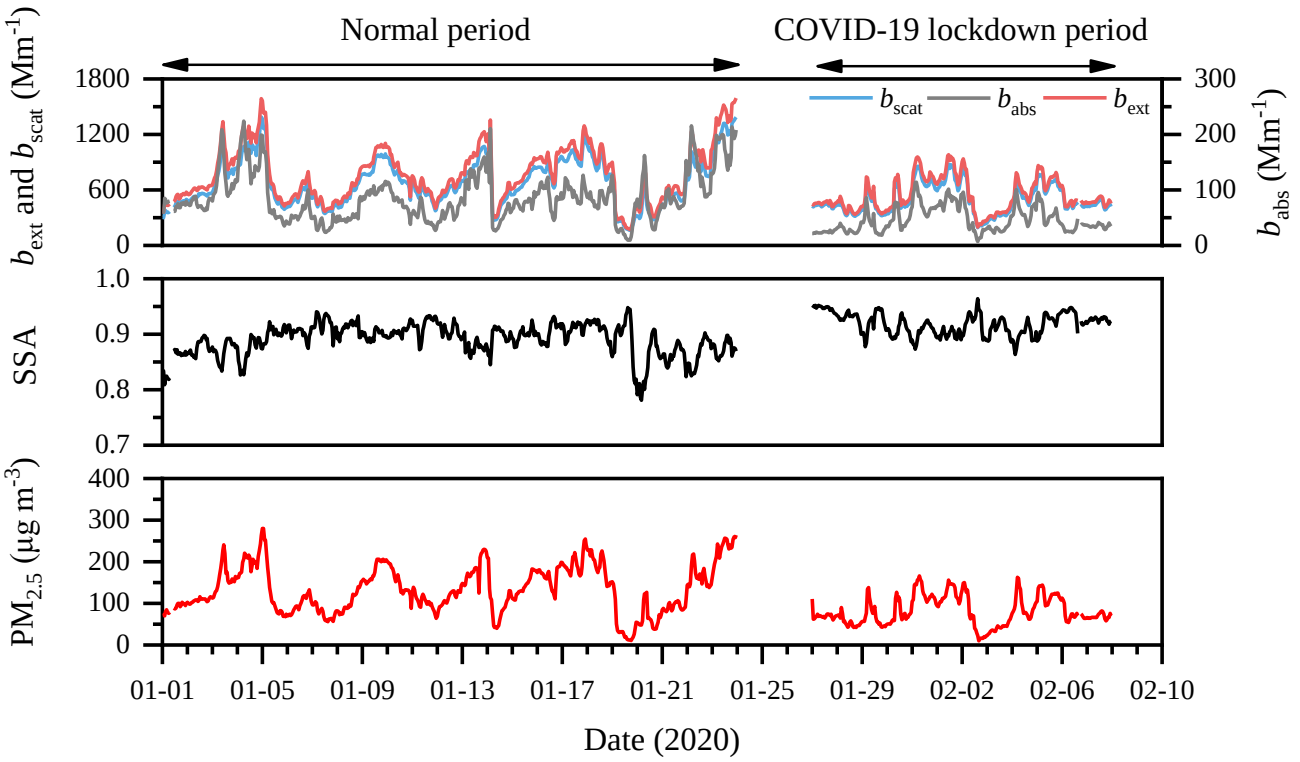

Figure 1. Hourly variations of light scattering (b_{scat}), absorption (b_{abs}), and extinction (b_{ext}) coefficients, single scattering albedo (SSA), and $PM_{2.5}$ mass concentrations in Xi'an during the normal (January 1st to 23rd, 2020) and COVID-19 lockdown (January 27th to February 7th, 2020) periods.

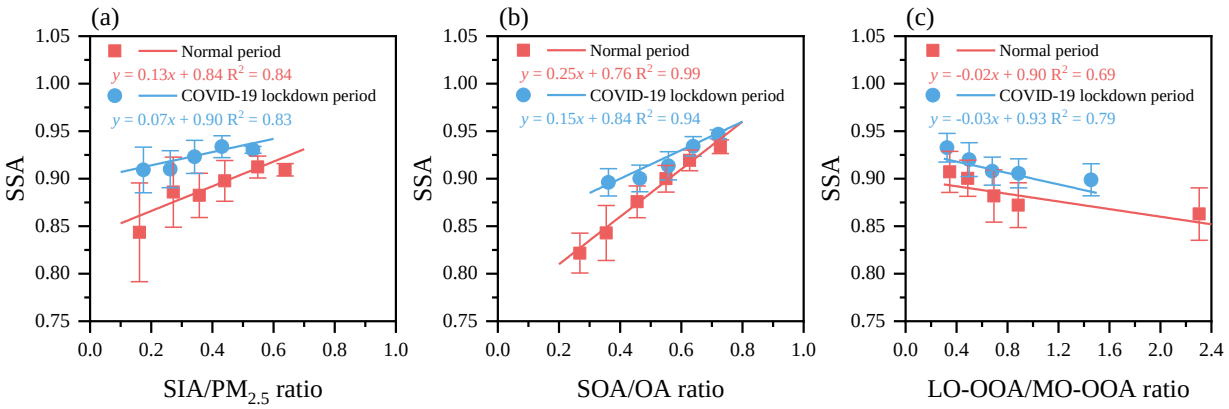

Figure 2. Variations of single scattering albedo (SSA) as a function of (a) secondary inorganic aerosol (SIA = NH_4NO_3 + $(NH_4)_2SO_4$)/$PM_{2.5}$, (b) secondary organic aerosol (SOA = LO-OOA + MO-OOA)/OA, and (c) LO-OOA/MO-OOA ratios during the normal and COVID-19 lockdown periods.

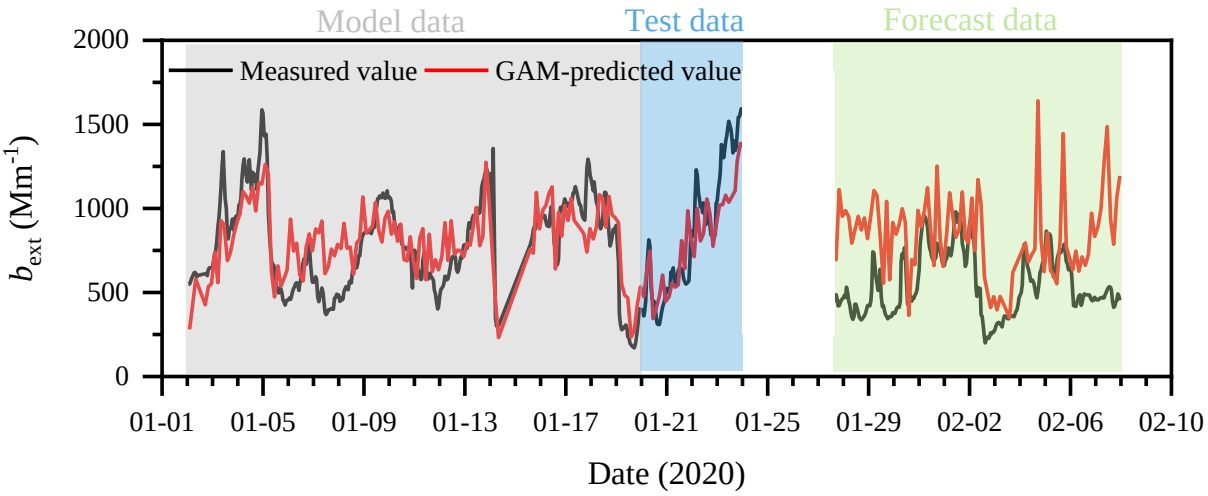

750

Figure 3. Time series of the measured and GAM-predicted light extinction coefficient (b_{ext}) for the model data, test data, and forecast data.

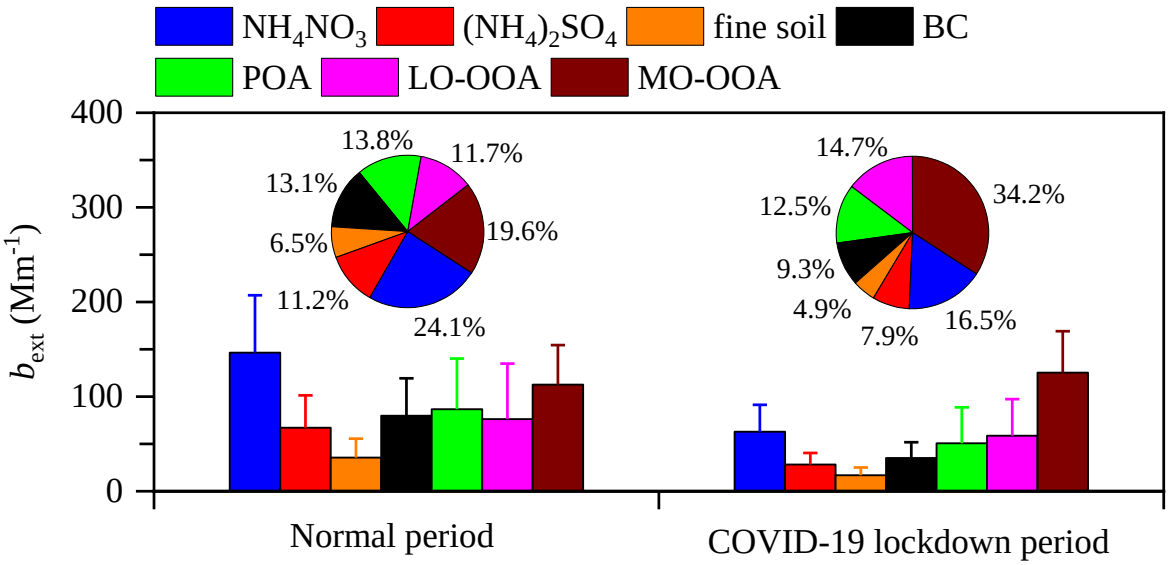

Figure 4. Contributions of NH_4NO_3, $(NH_4)_2SO_4$, fine soil, BC, POA, LO-OOA, and MO-OOA to the reconstructed chemical light extinction coefficient (b_{ext}) during the normal and COVID-19 lockdown periods.

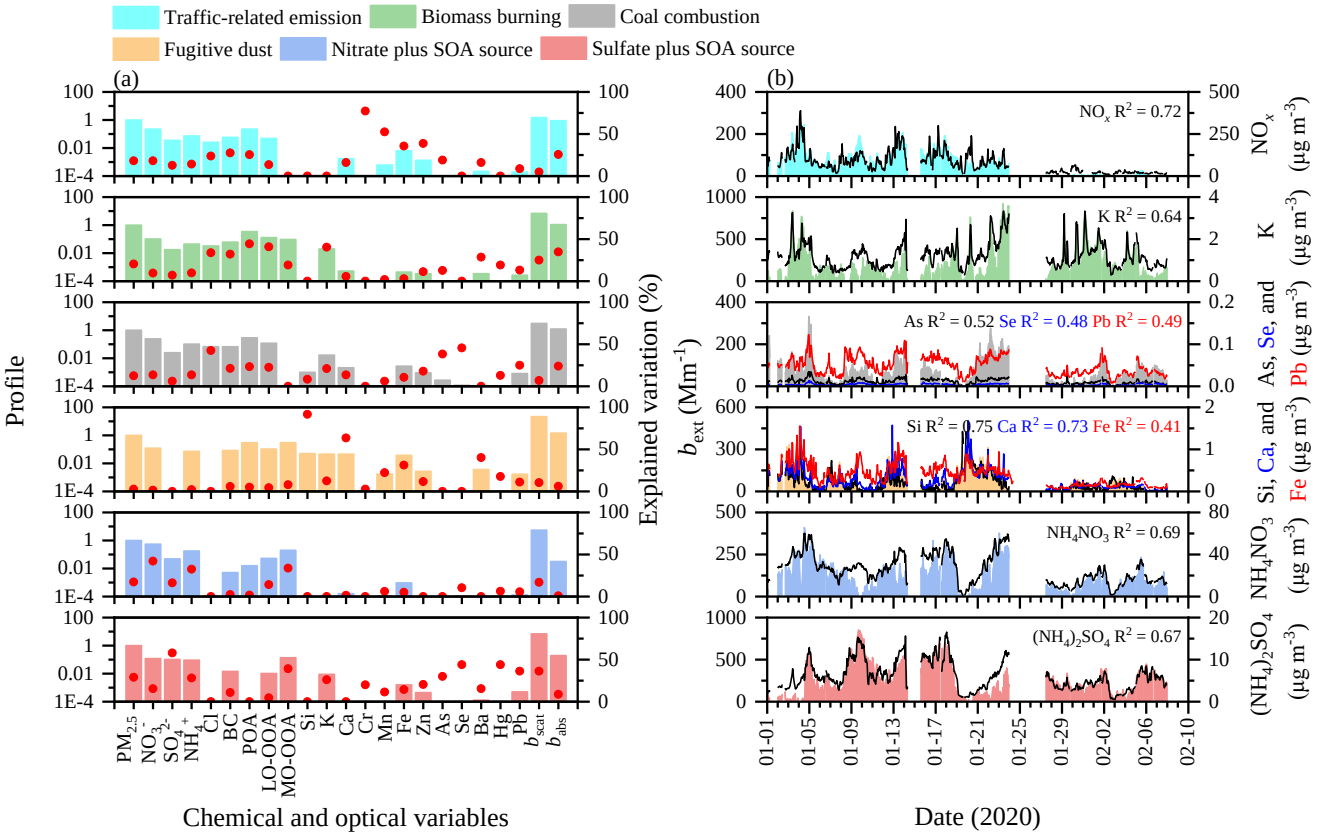

Figure 5. (a) Profiles and (b) time series plots of the resolved source factors in the six-factor solution, including traffic-related emission, biomass burning, coal combustion, fugitive dust, nitrate plus SOA source, and sulfate plus SOA source. The columns in each factor are the profile that displays the relative relation of absolute values of variables. The red dot represents the explained variation of species for different factors. The corresponding time trends of chemical tracers are also shown.

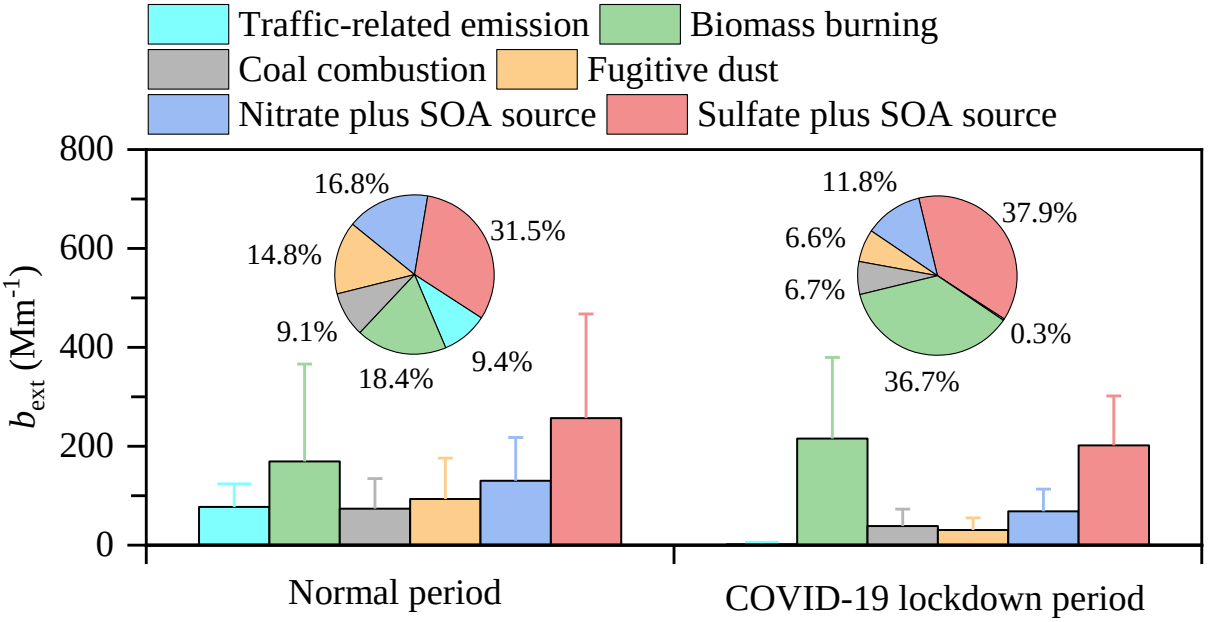

765 **Figure 6.** Contributions of six resolved sources to the modeled source light extinction coefficient (b_{ext}) during the normal and COVID-19 lockdown periods, including traffic-related emission, biomass burning, coal combustion, fugitive dust, nitrate plus SOA source, and sulfate plus SOA source.

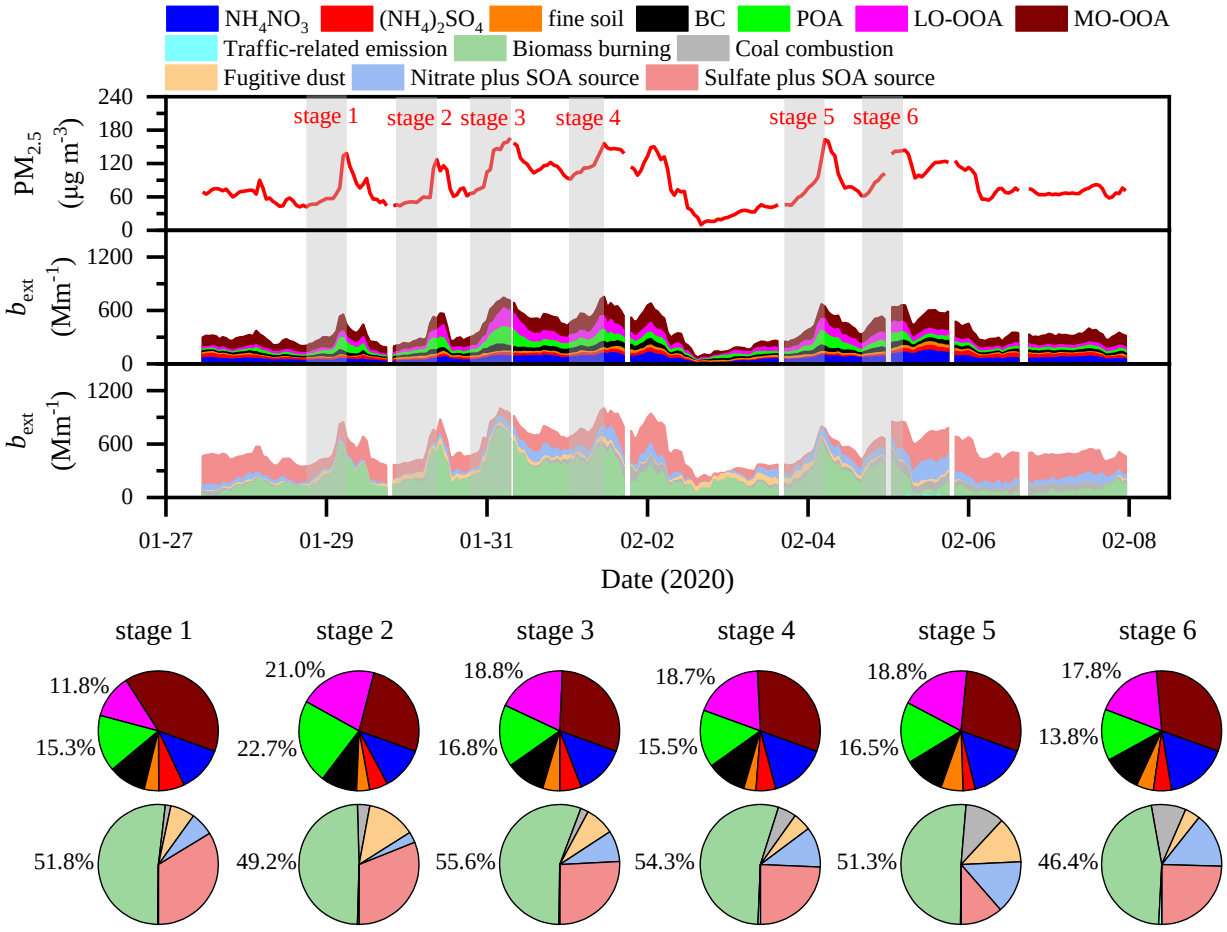

Figure 7. Time series of $PM_{2.5}$ mass concentration, the light extinction coefficient (b_{ext}) of chemical species, and the b_{ext} from six resolved sources during the lockdown period. Pie charts depicting the average fractional contributions of chemical species and sources to b_{ext} during the $PM_{2.5}$ rising stages, which were marked in light gray.

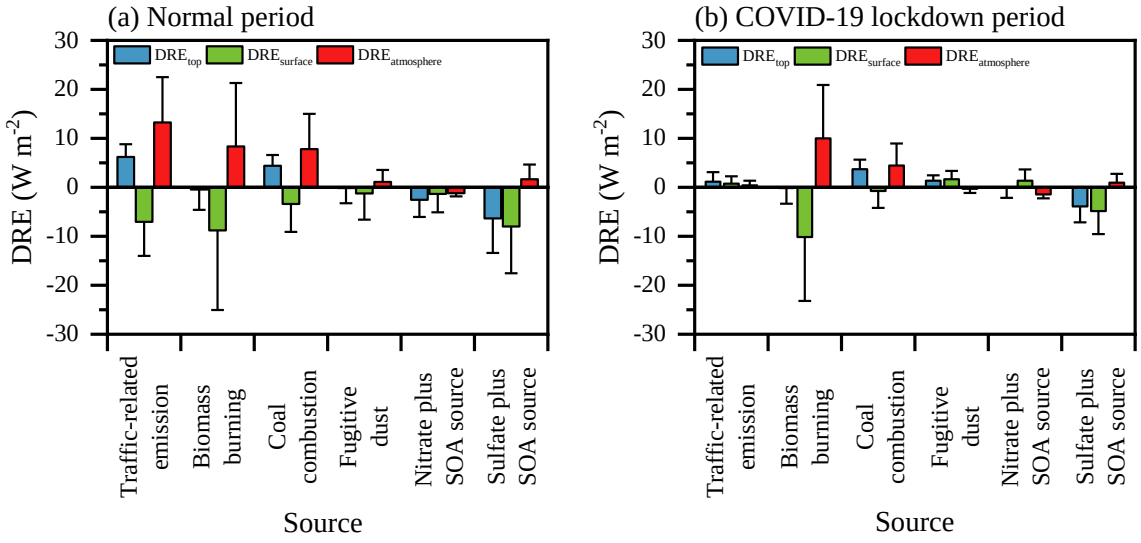

775 **Figure 8.** Direct radiative effect (DRE) of aerosol from traffic-related emission, biomass burning, coal combustion, fugitive dust, nitrate plus SOA source, and sulfate plus SOA source at the earth's surface, the top of the atmosphere, and in the atmosphere during the normal (a) and COVID-19 lockdown (b) periods.

Supplement of

Measurement report: The importance of biomass burning in light extinction and direct radiative effect of urban aerosol during the COVID-19 lockdown in Xi'an, China

Jie Tian[1,2], Qiyuan Wang[1,2,3], Huikun Liu[1], Yongyong Ma[4], Suixin Liu[1,2], Yong Zhang[1], Weikang Ran[1], Yongming Han[1,2,3], and Junji Cao[5]

[1]State Key Laboratory of Loess and Quaternary Geology, Institute of Earth Environment, Chinese Academy of Sciences, Xi'an 710061, China
[2]CAS Center for Excellence in Quaternary Science and Global Change, Xi'an 710061, China
[3]National Observation and Research Station of Regional Ecological Environment Change and Comprehensive Management in the Guanzhong Plain, Shaanxi, Xi'an 710061, China
[4]Meteorological Institute of Shaanxi Province, Xi'an 710015, China
[5]Institute of Atmospheric Physics, Chinese Academy of Sciences, Beijing 100029, China

Correspondence: Qiyuan Wang (wangqy@ieecas.cn) and Junji Cao (jjcao@mail.iap.ac.cn)

Text S1. Absorption Ångström exponent method

In this study, aerosol light absorption coefficient (b_{abs}) at wavelengths of λ = 370 nm, 470 nm, 520 nm, 590 nm, 660 nm, and 880 nm were measured by a newly developed Aethalometer (model AE33, Magee Scientific, Berkeley, CA, USA). The Absorption Ångström exponent (AAE) describes the wavelength dependence of aerosol light absorption and can be calculated according to power law fitting b_{abs} at wavelengths of 370 nm to 880 nm (Moosmüller et al., 2011) as below:

$$b_{abs}(\lambda) \sim \lambda^{-AAE} \quad (1)$$

Through the AAE method (Lack and Langridge, 2013), the mass absorption efficiency (MAE) of black carbon (BC) at 520 nm can be obtained as follows:

$$b_{abs}(520\ nm) = b_{abs\text{-}BC}(520\ nm) + b_{abs\text{-}BrC}(520\ nm) \quad (2)$$

$$b_{abs\text{-}BC}(520\ nm) = b_{abs\text{-}BC}(880\ nm) \times \left(\frac{520}{880}\right)^{-AAE_{BC}} \quad (3)$$

$$MAE_{BC}(520\ nm) = \frac{b_{abs\text{-}BC}(520\ nm)}{[BC]} \quad (4)$$

where b_{abs}-BC and b_{abs}-BrC in Mm^{-1} are the light absorption coefficients caused by BC and brown carbon (BrC), respectively; AAE_{BC} is the AAE caused by the BC particle, which can vary from 0.8 to 1.4 due to core size, coating materials, and mixing state (Lack and Cappa, 2010; Lack and Langridge, 2013). The linear relationship between the AAEs and the mass concentration ratios of organic aerosol (OA) to BC is investigated to find the realistic AAE_{BC} during the normal and lockdown periods (Figure S12) (Yuan et al., 2016); and [BC] is the mass concentration of BC in $\mu g\ m^{-3}$.

Text S2. Uncertainty of the element concentration

Considering the element concentration measured by the Xact 625 ambient metals monitor with a 1-hour sampling interval, the uncertainty of the element concentration (u_e) inputting into the receptor model was estimated as follows (Norris et al., 2014):

$$u_e = \sqrt{(c_e \times 10\%)^2 + (0.5 \times MDL)^2}, \text{ for } c_e > MDL \quad (5)$$

$$u_e = \frac{5}{6} \times MDL, \text{ for } c_e \leq MDL \quad (6)$$

where c_e is the concentration of the element; 10% is the default analytical relative error (Rai et al., 2020); and MDL represents the method detection limit of the element.

Text S3. Diagnostics of HERM solutions

In this study, factor numbers from two to eight were selected to run in the HERM software. Each factor solution was performed with completely unconstrained profiles at twenty different seeds to explore the possible sources. Detailed information on how the most interpretable factors were selected is presented below.

As shown in Figure S2, the values of Q/Q_{exp} (> 1) decreased as the factor numbers increased. The large Q/Q_{exp} values in two- (21.10 ± 0.03) and three-factor (12.29 ± 0.01) solutions indicated too few factors were resolved. In the four-factor solution (Figure S3), Factor 2 identified as biomass burning was characterized by high explained variations (EV) values of POA (56%), LO-OOA (54%), BC (43%), Cl (55%). Factor 3 was regarded as fugitive dust due to significant EV values of Si (100%), Ca (68%), and Fe (35%). For the Factor 4 assigned to the secondary source, EV values of NO_3^-, SO_4^{2-}, NH_4^+, and MO-OOA were larger than 30%. It is noted that Factor 1 was associated with the traffic-like source because b_{ext} from this source showed a moderate correlation with NO_x, a tracer of fresh motor vehicle exhaust emission ($R^2 = 0.58$). However, the high EV values of some specific elements (e.g., As (44%) and Se (31%)) in this factor indicated the possible mixture of other fossil fuel sources (e.g., coal combustion). When five factors were resolved, except traffic-like source (Factor 1), biomass burning (Factor 2), and fugitive dust (Factor 3), the secondary source was split into nitrate plus SOA (Factor 4) and sulfate plus SOA (Factor 5) sources (Figure S4). The increase to six-factor solution (Figure S5) showed well separation of traffic-related emission (Factor 1) and coal combustion (Factor 3). A stronger correlation between b_{ext} from traffic-related emission and NO_x ($R^2 = 0.72$) was found compared to traffic-like factors resolved in four– and five- factor solutions ($R^2 = 0.58$). As shown in Figures S6 and S7, further investigations of unconstrained profile solutions with seven and eight factors resulted in factor split. The extra split factors possibly came from biomass burning and coal combustion, mainly due to high EV values of K (26–33%), or As (21%). Despite b_{ext} from coal combustion factors in seven- and eight-factor solutions showed the stronger correlation with As ($R^2 = 0.63$–0.68), Se ($R^2 = 0.79$–0.86), and Pb ($R^2 = 0.60$–0.67), the profiles identified coal combustion had no POA contribution. Meanwhile, the values of POA in fugitive dust profiles identified in seven– and eight- factor solutions were higher than 1 (the reference standard of $PM_{2.5}$). It is indicated that these profiles did not match the real world.

Therefore, as the factor solutions described above, six factors were the most interpretable in our study, including traffic-related emission, biomass burning, coal combustion, fugitive dust, nitrate plus SOA source, and sulfate plus SOA source.

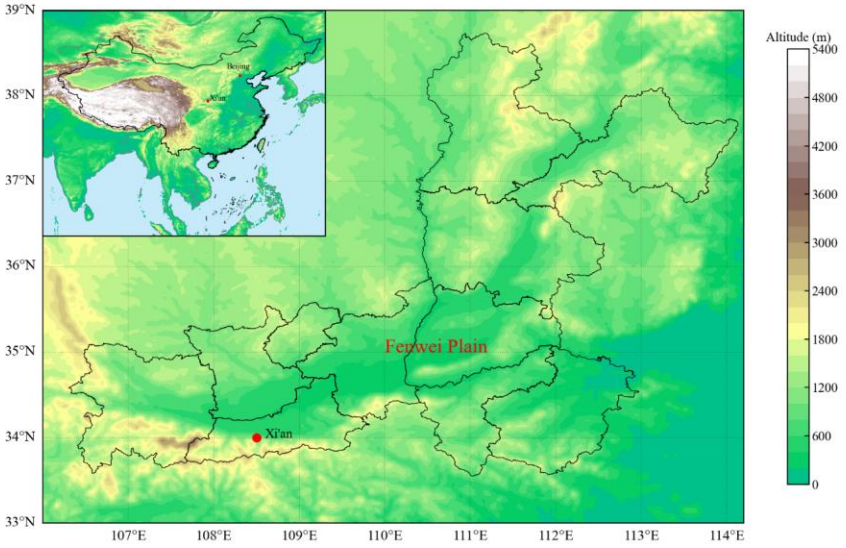

Figure S1. The location of the sampling site in Xi'an, China.

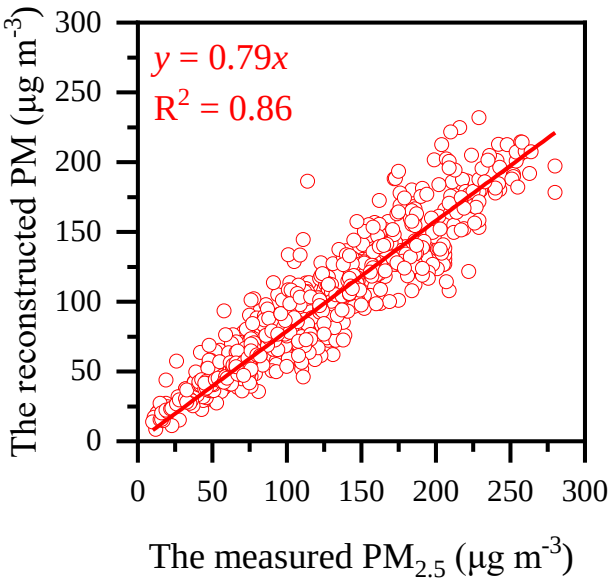

Figure S2. Linear relationship between the measured $PM_{2.5}$ concentration and the sum concentration of POA, LO-OOA, MO-OOA, NH_4NO_3, $(NH_4)_2SO_4$, BC, and fine soil (the sum is referred to as the reconstructed PM).

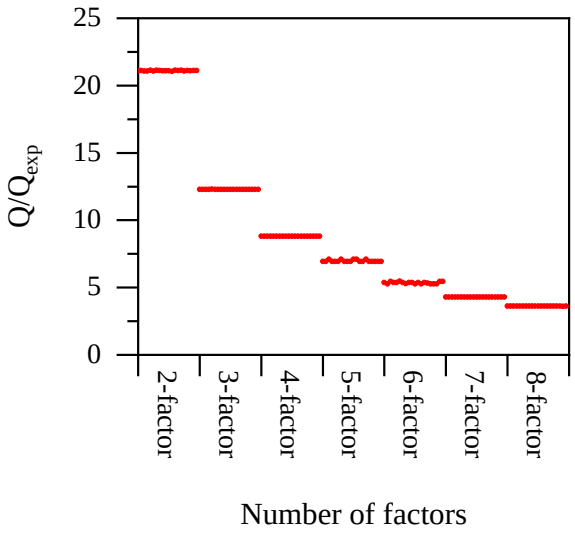

Figure ~~S2~~S3. Values of Q/Q_{exp} for the unconstrained profile solutions with two to eight factors at twenty different seeds.

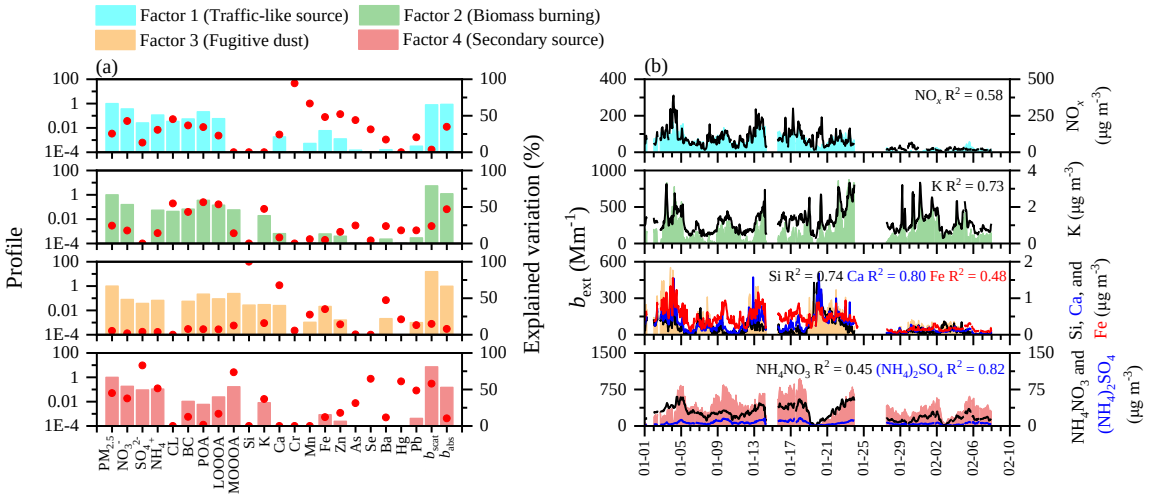

Figure ~~S3~~S4. (a) Profiles and (b) time series plots of the resolved source factors in the four-factor solution. The columns in each factor are the profile that displays the relative relation of absolute values of variables. The red dot represents the explained variation of species for different factors. The corresponding time trends of chemical tracers also are shown.

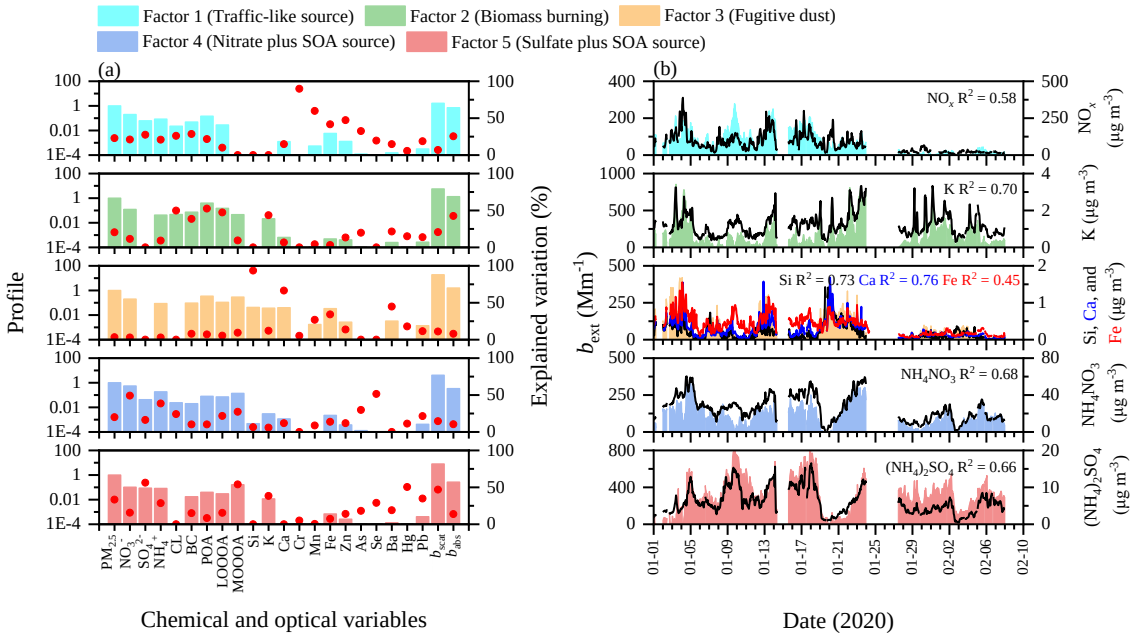

Figure ~~S4~~S5. (a) Profiles and (b) time series plots of the resolved source factors in the five-factor solution. The columns in each factor are the profile that displays the relative relation of absolute values of variables. The red dot represents the explained variation of species for different factors. The corresponding time trends of chemical tracers also are shown.

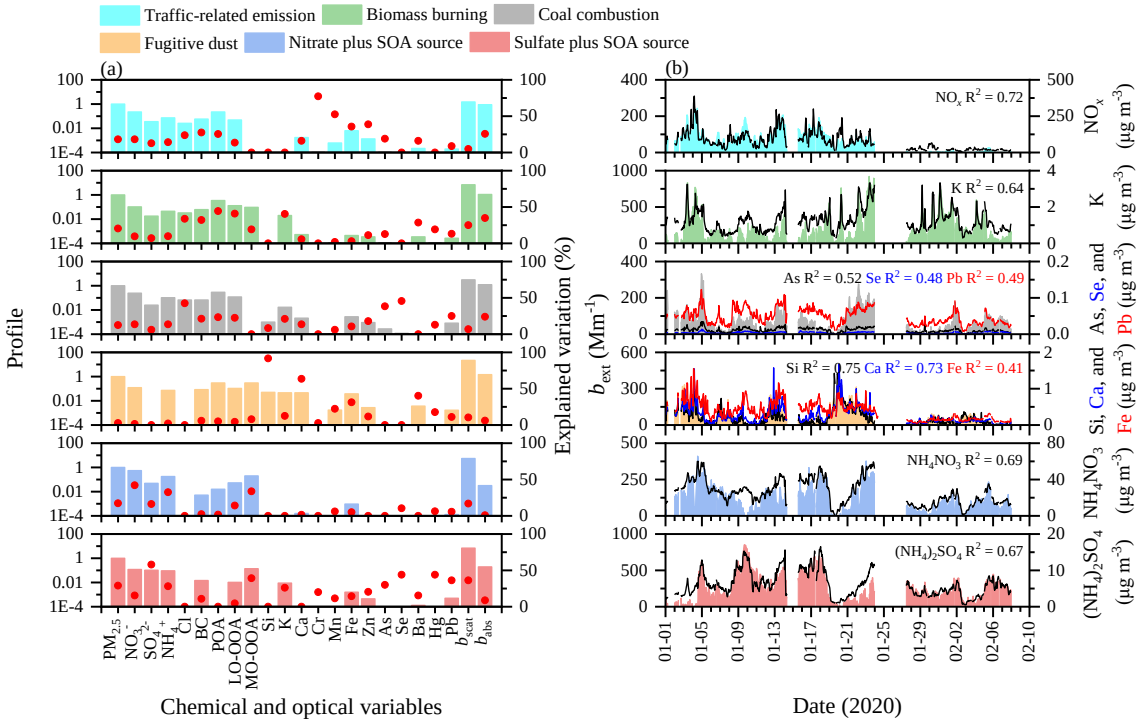

Figure ~~S5~~S6. (a) Profiles and (b) time series plots of the resolved source factors in the six-factor solution. The columns in each factor are the profile that displays the relative relation of absolute values of variables. The red dot represents the explained variation of species for different factors. The corresponding time trends of chemical tracers also are shown.

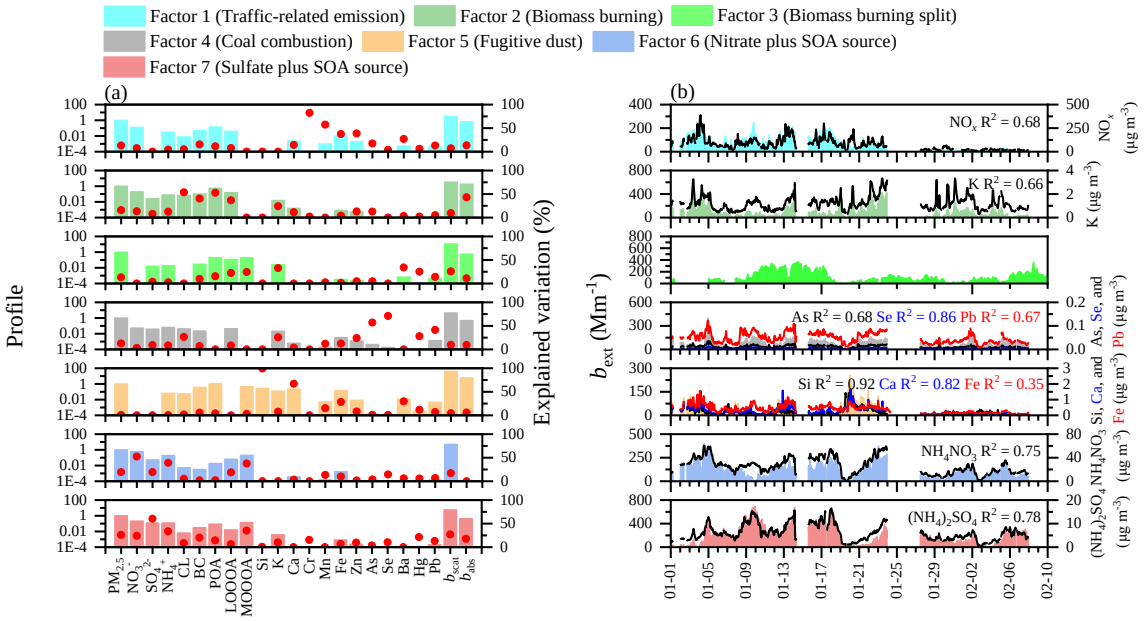

Figure ~~S6~~S7. (a) Profiles and (b) time series plots of the resolved source factors in the seven-factor solution. The columns in each factor are the profile that displays the relative relation of absolute values of variables. The red dot represents the explained variation of species for different factors. The corresponding time trends of chemical tracers also are shown.

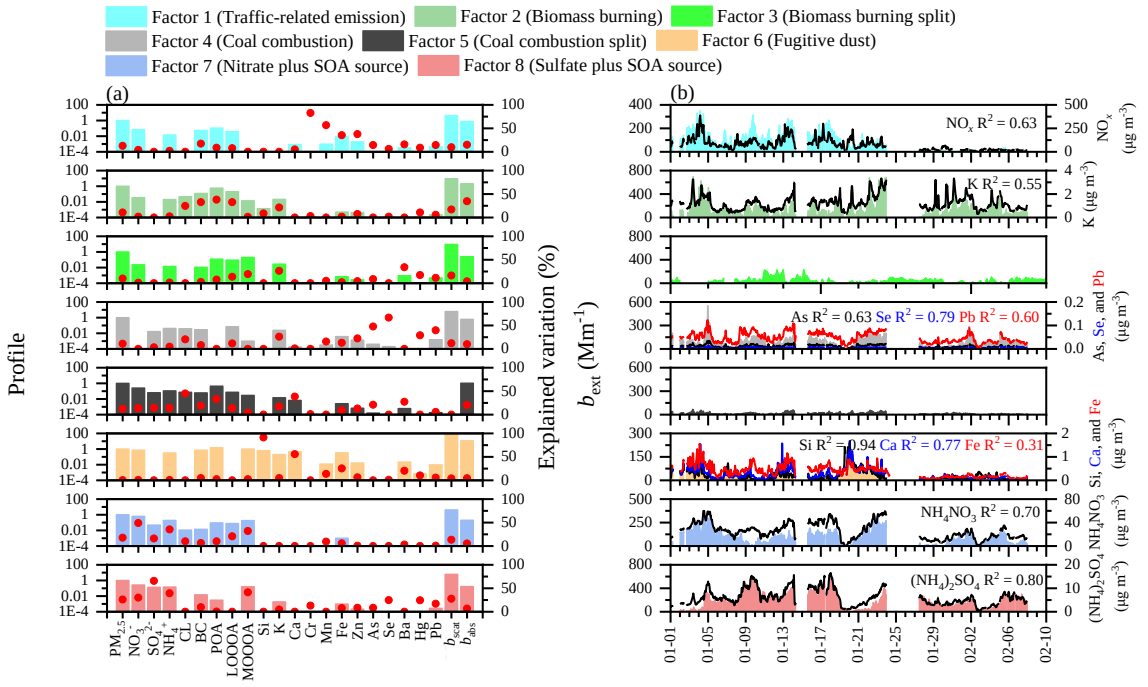

Figure ~~S7~~S8. (a) Profiles and (b) time series plots of the resolved source factors in the eight-factor solution. The columns in each factor are the profile that displays the relative relation of absolute values of variables. The red dot represents the explained variation of species for different factors. The corresponding time trends of chemical tracers also are shown.

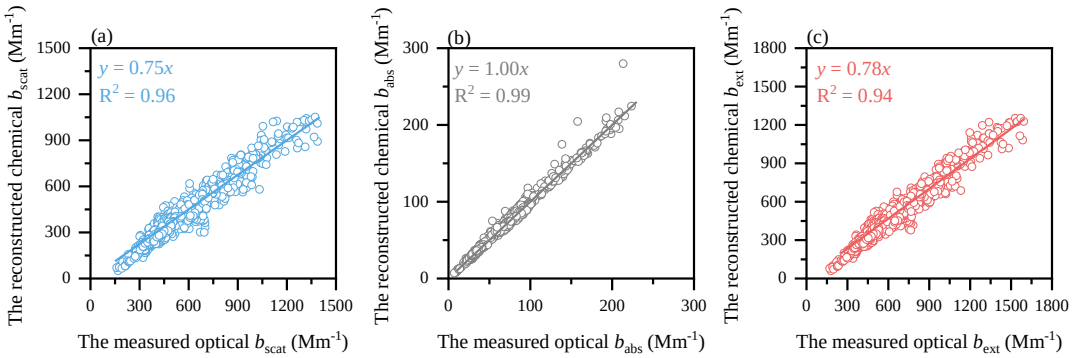

Figure S98. Linear relationships between the reconstructed chemical and the measured optical (a) b_{scat}, (b) b_{abs}, and (c) b_{ext}.

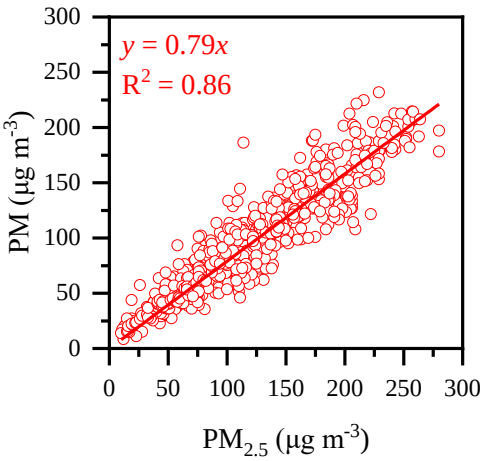

Figure S9. Linear relationship between $PM_{2.5}$ and PM used in the reconstruction of aerosol optical coefficients. PM is the sum of NH_4NO_3, $(NH_4)_2SO_4$, fine soil, BC, POA, LO-OOA, and MO-OOA in this study. The slope of the linear regression between $PM_{2.5}$ and PM concentrations (0.79) was close to that between the measured optical b_{ext} and the reconstructed chemical b_{ext} (0.78, see Figure S8c), suggesting that chemical calculation of b_{ext} was a reasonable estimation of aerosol optical coefficients by using chemical components data.

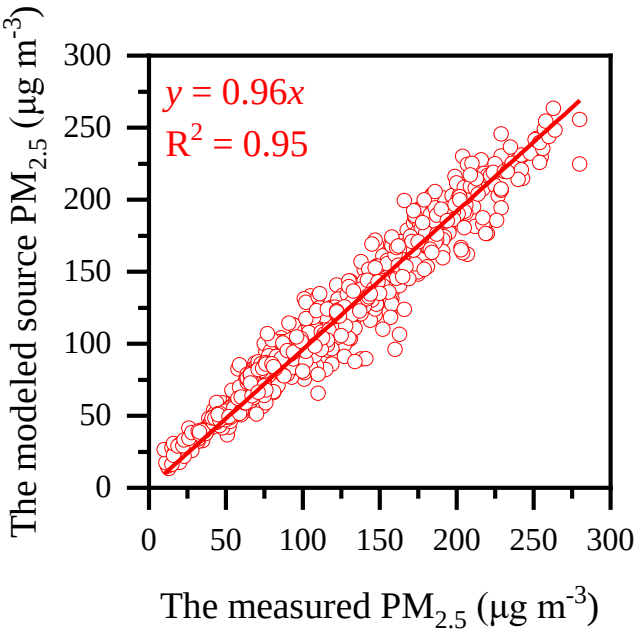

Figure S10. Linear relationship between the modeled source and the measured $PM_{2.5}$ mass concentration. The modeled source $PM_{2.5}$ was strongly correlated linearly with the measured optical $PM_{2.5}$ (R^2 = 0.95, slope = 0.96), indicating that the six identified sources can adequately account for the variability in $PM_{2.5}$ mass concentration.

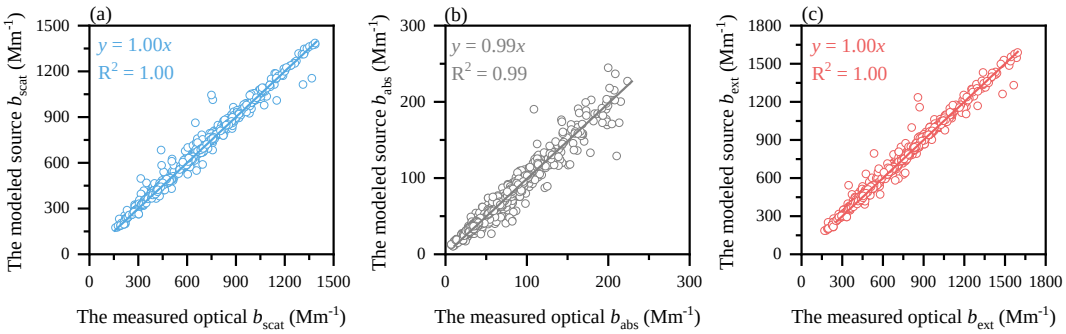

134

135 **Figure S11.** Linear relationships between the modeled source and the measured optical (a) b_{scat}, (b) b_{abs},
136 and (c) b_{ext}. The modeled source b_{scat}, b_{abs}, and b_{ext} were strongly correlated linearly with the measured
137 optical b_{scat} (R^2 = 1.00, slope = 1.00), b_{abs} (R^2 = 0.99, slope = 0.99), and b_{ext} (R^2 = 1.00, slope = 1.00),
138 indicating that the six identified sources can adequately account for the variability in aerosol optical
139 coefficients.

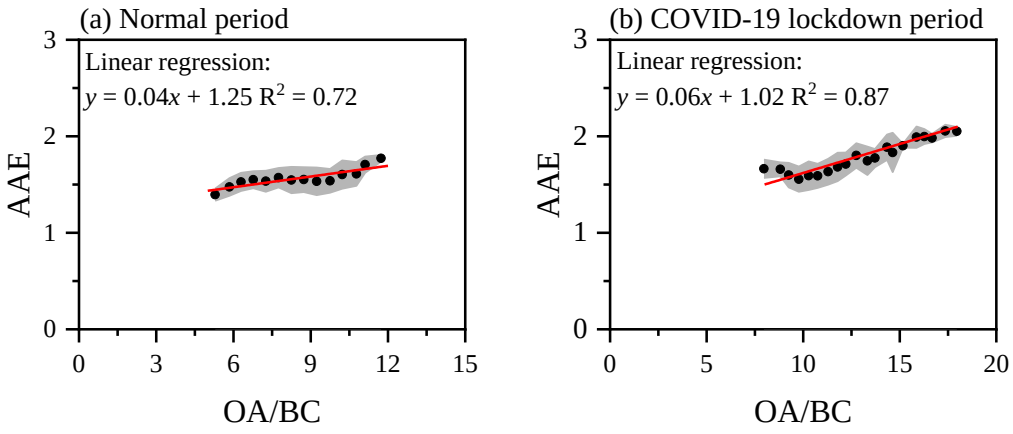

Figure S12. Linear relationships between the AAEs and the mass concentration ratios of organic aerosol (OA) to BC (OA/BC) during the normal (a) and lockdown (b) periods. The intercept of the linear regression represents the realistic AAE_{BC}. The points and light gray shadows represent the mean values and error margins in each bin (Δ(OA/BC) = 0.5).

Table S1. Summary of chemical and meteorological measurements of in Xi'an before and during the COVID-19 lockdown period.

Parameters	Sampling interval	Instruments and online source	Operation and calibration
Chemical variables			
NO_3^-, SO_4^{2-}, NH_4^+, Cl^-, and OA	15-min	Quadrupole aerosol chemical speciation monitor (Q-ACSM, Aerodyne Research Inc., Billerica, Massachusetts, USA)	The relative ionization efficiencies (RIEs) for OA, nitrate, and chloride were set to 1.4, 1.1, and 1.3 by default, respectively. The RIE for ammonium (5.8) was determined from the ammonium nitrate aerosol calibration, while the RIE for sulfate (1.9) was estimated by fitting the measured sulfate versus predicted sulfate values. The collection efficiency was set to 0.45.
Si, K, Ca, Cr, Mn, Fe, Zn, As, Se, Ba, Hg, and Pb	1-hour	Xact 625 ambient metals monitor (Xact 625i, Cooper Environmental Services, Beaverton, OR, USA)	Daily advanced quality assurance checks were performed during 30 min after midnight to monitor shifts in the calibration.
$PM_{2.5}$ and NO_x	5-min	The Department of Ecology and Environment of Shaanxi Province (http://sthjt.shaanxi.gov.cn, in Chinese)	
Meteorological variables*			
WS, WD, T, P, and DP	1-hour	Integrated automatic weather station (MAWS201, Vaisala, Helsinki, Finland)	
PBLH	3-hour	Global Data Assimilation System (ftp://arlftp.arlhq.noaa.gov/pub/archives/gdas1)	PBLH at the sampling site was obtained using linear interpolation method.

*WS, WD, T, P, DP, and PBLH represent wind speed, wind direction, temperature, pressure, dew point, and planetary boundary layer height, respectively.

149 **Table S2.** Summary of output indices from the constructed b_{ext} GAM.

Intercept	6.64	
Adjusted R^2	0.54	
Smoothed parameters*	F value	*p* value
f(WS)	3.402	0.002331
f(WD)	5.820	0.000134
f(T)	2.707	0.012809
f(P)	3.209	0.001757
f(DP)	13.325	$< 2.00 \times 10^{-16}$
f(PBLH)	3.656	0.026822

150 *WS, WD, T, P, DP, and PBLH represent wind speed, wind direction, temperature, pressure, dew point,
151 and planetary boundary layer height, respectively.

Table S3. Concurvity indices between each independent smoothed parameter in the constructed GAM.

Smoothed parameters*	*f*(WS)	*f*(WD)	*f*(T)	*f*(P)	*f*(DP)	*f*(PBLH)
f(WS)	1.00	0.28	0.03	0.09	0.07	0.23
f(WD)	0.15	1.00	0.08	0.09	0.03	0.07
f(T)	0.06	0.07	1.00	0.11	0.25	0.22
f(P)	0.08	0.24	0.08	1.00	0.06	0.09
f(DP)	0.05	0.06	0.08	0.07	1.00	0.05
f(PBLH)	0.13	0.07	0.05	0.04	0.06	1.00

*WS, WD, T, P, DP, and PBLH represent wind speed, wind direction, temperature, pressure, dew point, and planetary boundary layer height, respectively.

References

Lack, D. A. and Cappa, C. D.: Impact of brown and clear carbon on light absorption enhancement, single scatter albedo and absorption wavelength dependence of black carbon, Atmos. Chem. Phys., 10, 4207–4220, https://doi.org/10.5194/acp-10-4207-2010, 2010.

Lack, D. A. and Langridge, J. M.: On the attribution of black and brown carbon light absorption using the Ångström exponent, Atmos. Chem. Phys., 13, 10535–10543, https://doi.org/10.5194/acp-13-10535-2013, 2013.

Moosmüller, H., Chakrabarty, R. K., Ehlers, K. M., and Arnott, W. P.: Absorption Ångström coefficient, brown carbon, and aerosols: basic concepts, bulk matter, and spherical particles, Atmos. Chem. Phys., 11, 1217–1225, https://doi.org/10.5194/acp-11-1217-2011, 2011.

Norris, G., Duvall, R., Brown, S., and Bai, S.: EPA positive matrix factorization (PMF) 5.0 fundamentals and user guide, 2014.

Rai, P., Furger, M., Slowik, J. G., Canonaco, F., Fröhlich, R., Hüglin, C., Minguillón, M. C., Petterson, K., Baltensperger, U., and Prévôt, A. S. H.: Source apportionment of highly time-resolved elements during a firework episode from a rural freeway site in Switzerland, Atmos. Chem. Phys., 20, 1657–1674, https://doi.org/10.5194/acp-20-1657-2020, 2020.

Yuan, J. F., Huang, X. F., Cao, L. M., Cui, J., Zhu, Q., Huang, C. N., Lan, Z .J., and He, L. Y.: Light absorption of brown carbon aerosol in the PRD region of China, Atmos. Chem. Phys., 16, 1433–1443, https://doi.org/10.5194/acp-16-1433-2016, 2016.